

Ongoing postseismic vertical deformation of the Australian continent from far-field earthquakes

Anna Riddell¹, Matt King², and Christopher Watson²

¹Geoscience Australia, University of Tasmania

²University of Tasmania

November 24, 2022

Abstract

We use GPS observations to investigate the magnitude and spatial distribution of vertical coseismic and postseismic deformation of the Australian continent and compare these with elastic and viscoelastic model outputs. We observe and model surface deformation in Australia caused by six recent large far-field events: 2004 Mw 8.1 Macquarie Ridge, 2004 Mw 9.3 Sumatra-Anderman, 2005 Mw 8.6 in northern Sumatra, the 2007 series of Mw 8.5 and 7.9 in southern Sumatra, two events in 2012 of Mw 8.6 and 8.2 in northern Sumatra, and the 2009 Mw 7.8 south of New Zealand. Observed vertical coseismic deformation reaches 3 mm, with the magnitude varying spatially and by earthquake in broad agreement with modelling of coseismic deformation. Postseismic deformation is observed in all three coordinate components at Australian GPS sites nearest to these earthquakes, with deformations reaching several mm/yr in the vertical over multiple years. In particular, the Sumatran sequence produces observed subsidence in north-western Australia of up to 4 mm/yr over 2004.9-2010.0 where predictions based on one-dimensional viscoelastic Earth models replicate the subsidence but underpredict the vertical rate by a factor of two. Across all earthquakes, the models often fit one or two coordinate components of the observations, but rarely all three. Unmodeled lateral rheological structure likely contributes to this given the difference between the oceanic location of the earthquakes and the Australian continental setting of the GPS sites. The magnitude and spatial extent of these coseismic and postseismic deformations warrant their consideration in future updates of the geodetic terrestrial reference frame.

Hosted file

essoar.10504158.1.docx available at <https://authorea.com/users/549816/articles/603748-ongoing-postseismic-vertical-deformation-of-the-australian-continent-from-far-field-earthquakes>

Hosted file

supporting_information_postseismic_riddell_king_watson.docx available at <https://authorea.com/users/549816/articles/603748-ongoing-postseismic-vertical-deformation-of-the-australian-continent-from-far-field-earthquakes>

1 **Ongoing postseismic vertical deformation of the Australian continent from far-field**
2 **earthquakes**

3 Anna R. Riddell^{1,2}, Matt A. King¹, Christopher S. Watson¹

4 ¹School of Technology, Environments and Design, University of Tasmania, Hobart, Australia

5 ²Geoscience Australia, Canberra, Australia

6 Corresponding author: Anna Riddell, Anna.Riddell@ga.gov.au, +61 2 6249 9359

7 Submitted: 17 June 2020

8 Abbreviated title: Postseismic deformation in Australia

9 Key Points:

- 10 • Vertical postseismic deformation of the Australian continent, induced by large far-field
- 11 earthquakes, is investigated using GPS and forward modelling
- 12 • Postseismic subsidence reaches 4-5mm/yr over several years, most notable following the
- 13 Sumatran earthquake sequence
- 14 • Predictions based on 1D viscoelastic Earth models replicate the subsidence but
- 15 underpredicts the vertical rate by a factor of two

16 Key Words: GPS time series, coseismic offset, postseismic deformation, Australia, vertical land
17 motion

18 GJI key words: loading of the Earth, satellite geodesy, reference systems, plate motions, transient
19 deformation, Australia

20 **Abstract**

21 We use GPS observations to investigate the magnitude and spatial distribution of vertical coseismic
22 and postseismic deformation of the Australian continent and compare these with elastic and
23 viscoelastic model outputs. We observe and model surface deformation in Australia caused by six
24 recent large far-field events: 2004 M_w 8.1 Macquarie Ridge, 2004 M_w 9.3 Sumatra-Anderman, 2005
25 M_w 8.6 in northern Sumatra, the 2007 series of M_w 8.5 and 7.9 in southern Sumatra, two events in
26 2012 of M_w 8.6 and 8.2 in northern Sumatra, and the 2009 M_w 7.8 south of New Zealand. Observed
27 vertical coseismic deformation reaches 3 mm, with the magnitude varying spatially and by
28 earthquake in broad agreement with modelling of coseismic deformation. Postseismic deformation
29 is observed in all three coordinate components at Australian GPS sites nearest to these earthquakes,
30 with deformations reaching several mm/yr in the vertical over multiple years. In particular, the
31 Sumatran sequence produces observed subsidence in north-western Australia of up to 4 mm/yr over
32 2004.9-2010.0 where predictions based on one-dimensional viscoelastic Earth models replicate the

33 subsidence but underpredict the vertical rate by a factor of two. Across all earthquakes, the models
34 often fit one or two coordinate components of the observations, but rarely all three. Unmodeled
35 lateral rheological structure likely contributes to this given the difference between the oceanic
36 location of the earthquakes and the Australian continental setting of the GPS sites. The magnitude
37 and spatial extent of these coseismic and postseismic deformations warrant their consideration in
38 future updates of the geodetic terrestrial reference frame.

39 1 Introduction

40 The conventional theory of plate tectonics suggests that earthquakes in their most simple form are a
41 result of the interaction between “rigid plates” (Müller and Seton, 2015). Being located far from
42 active plate boundaries, continental Australia experiences infrequent large-magnitude seismicity,
43 and hence very little intraplate crustal deformation, aside from instantaneous deformation due to
44 large and far-field plate-boundary earthquakes. However, the complex stress fields at plate
45 boundaries results in far-field deformations that have been observed across Australia in the
46 horizontal coordinate component (e.g. Burbidge, 2004, Kennett and Blewett, 2012, Tregoning et al.,
47 2013). Recent geodetic evidence has shown that plate interiors globally are deforming horizontally
48 due to near and far-field earthquakes, both co-seismically and post-seismically, including Australia
49 (e.g. King and Santamaría-Gómez, 2016, Tregoning et al., 2013).

50 The Australian continent is located entirely within the Indo-Australian plate (Figure 1), which has
51 been formerly labelled as a ‘plate of extremes’ (Keep and Schellart, 2012) due to the complex plate
52 boundary interactions. The plate boundary includes the large converging mountain range on the
53 north-western margin (the Himalayas); one of the largest convergent subduction zones (Sunda
54 megathrust) located along the north-eastern boundary; and the inclusion of one of the fastest
55 subduction zones on Earth (the Tonga-Kermadec-Hikurangi zone) along the eastern boundary (Bevis
56 et al., 1995). The variety of plate boundary interactions provides various mechanisms for significant
57 numbers of earthquakes, some with very large magnitudes.

58 Geodetic studies have shown non-negligible horizontal coseismic and postseismic deformation of
59 Australia (Tregoning et al., 2013) but these have not yet been extended to consider the vertical
60 component of coseismic and postseismic deformation. The theoretical potential for cumulative
61 horizontal coseismic deformation in Australia was highlighted by Métivier et al. (2014) to be ~1 cm
62 over the period 1991.0 – 2011.0, but there are no observational studies that have focused on
63 vertical coseismic deformation in Australia. As a result of mega-earthquakes, Trubienko et al. (2014)
64 showed that the accumulated postseismic deformation values in the far-field (500 – 1500 km) of the
65 Sumatra 2004, Chile 2010 and Japan 2011 earthquakes could be as large as the coseismic offsets
66 after 3 – 4 years of deformation with a tendency towards subsidence, but did not investigate sites in
67 Australia.

68 The deformation of the Earth's crust and mantle after an earthquake is a function of the earthquake
69 magnitude, the rheological structure of the solid Earth, and the geometry and mechanism of the
70 fault failure (strike direction, dip, rake, length, location). Geodetic point positioning systems, such as
71 GPS, can provide time series of site locations suitable to monitor crustal dynamics in space and time
72 (Bock and Melgar, 2016). Combined with geodetic observations, viscoelastic modelling of
73 postseismic deformation provided insights into the rheological structure of the mantle and
74 asthenosphere. Tregoning et al. (2013) assessed the global horizontal deformation field of 15 great
75 earthquakes ($M_w > 8.0$) over the period 2000.0-2011.0 and the postseismic deformation observed in
76 a subset of Australian GPS time series, but only presented results for the horizontal coordinate
77 components. Watson et al. (2010) studied the vertical deformation of the 2004 Macquarie Island
78 event at the MAC1 site, showing substantial vertical deformation at this near-field site, but did not
79 consider vertical deformation at other locations further north.

80 Postseismic surface deformation changes the surface trajectory of a site relative to its pre-
81 earthquake velocity, which if un-modelled in the GPS time series can bias geophysical interpretation
82 that otherwise assumes secular motions (Altamimi et al., 2016, Hearn, 2003). In the realization of

83 geodetic reference frames, like the International Terrestrial Reference Frame (ITRF), the GPS time
84 series are considered representative of observed surface motion and reflecting that motion in
85 models can be challenging given often poorly constrained fault parameters (Hearn et al., 2013).
86 Poorly constrained fault parameters are sometimes caused by the complexity of the fault geometry
87 or the remote location (and limited observation) of the earthquake event. Here we define transient
88 motion as a residual signal which is non-periodic and non-secular (e.g., Bedford and Bevis, 2018,
89 Walwer et al., 2016). Unmodelled deformations affect the accuracy of the terrestrial reference
90 frame, which is constructed from VLBI, SLR, GNSS and DORIS observations. Vertical postseismic
91 deformations, if identified, would need to be considered to meet the Global Geodetic Observing
92 System requirements of an accurate and reliable reference frame at the 1-millimetre level with the
93 desired goal of stability of 0.1 millimetres per year (Blewitt, 2015, Gross et al., 2009).

94 Globally, the dominant driver of vertical land motion over centuries to millennia is glacial isostatic
95 adjustment (GIA). Predictions of GIA-induced vertical land motion from different GIA models show
96 discrepancies at the level of up to a few millimetres per year globally (e.g., Oostanciaux et al., 2012),
97 but the magnitude of the signal across the Australian landmass is in the range of ± 0.5 mm/yr (Riddell
98 et al., 2020). In contrast, current GPS observations, spanning 15 years at a dozen permanently
99 operating sites in Australia suggest that the continent is subsiding at the rate of ~ 1.0 mm/yr
100 (Altamimi et al., 2016, Burgette et al., 2013, King et al., 2012, Santamaría-Gómez et al., 2012,
101 Schumacher et al., 2018). Pfeffer et al. (2017) compared land motion measured as a difference
102 between altimetry and tide gauge observations with predicted land motion from surface mass
103 loading and present day ice-mass changes showing significant disagreement at the level of 1-2
104 mm/yr, again suggesting increased subsidence around the Australian coastline from observations
105 compared to models. Pfeffer et al. (2017) attributed the difference between observed and predicted
106 rates of land motion to be linked to an assumption of continental tilt and dynamic topography (e.g.
107 Heine et al., 2010, Sandiford, 2007), which supports their finding of greater uplift rates in southeast
108 Australia. These differences between geodetic measurements and GIA models have, thus far, not

109 been clearly attributed to a geophysical origin or systematic error (Riddell et al., 2020), but broad-
110 wavelength deformation, such as far-field postseismic motion could be a contributor.

111 In this paper, we investigate non-linear deformation induced by a selection of recent and historic
112 earthquakes, taking into consideration far-field effects from large plate boundary earthquake events
113 in the Australian region. Our focus is on the thus-unexplored vertical component but we also
114 consider the horizontal components of deformation. In this paper we consider a representative
115 selection of recent large earthquakes in various locations in the Australian region (northwest and
116 southeast of Australia). Time series from GNSS sites in the Australian AuScope network over the
117 period 2000.0-2019.0 are used (Figure 1, see also Table S1). We further extend the study backward
118 in time to consider the effects of large earthquakes pre-GPS on present-day deformation, based on
119 two events south of New Zealand.

120 2 Recent earthquakes and observed deformation in the Australian 121 region

122 To address the question of deformation of the Australian continent from far-field events we select
123 seven representative events, detailed in Table 1 and their locations shown in Figure 1. We do not
124 attempt to consider all events that have occurred in the geodetic period, rather we consider some of
125 the most significant plate boundary earthquakes over the time period 2004.0 – 2013.0. This time
126 period allows us enough data span and spatial density of GPS observations before and after each
127 earthquake to define changes in surface velocity associated with each earthquake. In the following
128 sections, we briefly detail each earthquake.

129 2.1 Puysegur Trench 1979 & 2009 (PT79, PT09)

130 The M_w 7.8 2009 event occurred off the west coast of the South Island of New Zealand (Figure 1) on
131 15 July at a depth of 12 km. The earthquake occurred along the boundary of the Indo-Australian and
132 Pacific plates and was the result of shallow thrust faulting. Faulting along this margin is

133 accommodated by oblique convergence at the Puysegur Trench as the Indo-Australian plate
134 subducts beneath the Pacific plate (Beavan et al., 2010, Hayes et al., 2009, Hayes et al., 2017).
135 Estimates of fault depth, orientation and location suggested that the slip occurred on the subduction
136 thrust interface between the Indo-Australian and Pacific plates (Hayes et al., 2017). Maximum slip
137 estimates are 5-6 m over a subduction interface patch of 80 by 50 km (Beavan et al., 2010).
138 On 12 October 1979 a M_w 7.4 event (Webb and Lowry, 1982) occurred in a similar location under
139 similar subduction circumstances to the 2009 event (Figure 1), showing active subduction on an east-
140 dipping thrust with a reverse faulting mechanism (Anderson et al., 1993). Approximately 110 km
141 separates the surface location of the 2009 and 1979 epicentres. The 1979 event predates the
142 commencement of the continuous GPS record in Australia (in 1996) by approximately 17 years and
143 the VLBI record by three years.

144 2.2 Macquarie Ridge 2004 (MI04)

145 On 23 December 2004, a M_w 8.1 earthquake occurred within the Indo-Australian plate on the
146 Macquarie Ridge (Figure 1). This event was the result of a rupture along a shallow left-lateral south-
147 southeast strike-slip fault with approximate dimensions of 140 km x 20 km (length x width) (Hayes et
148 al., 2017). Watson et al. (2010) provide a set of fault parameters derived using coseismic estimates
149 from GPS and seismic locations. These were then refined by Tregoning et al. (2013) using an updated
150 slip inversion and then further refined by King and Santamaría-Gómez (2016).

151 2.3 Sumatra-Anderman 2004 (SU04)

152 Three days after the MI04 event, on 26 December 2004, one of the largest earthquakes on record
153 (M_w 9.3) occurred along the intersection of the India plate and the Burma microplate, rupturing
154 along a zone 1300 km in length. The event was as a result of thrust faulting (Hayes et al., 2017). Fault
155 rupture parameters are used from Banerjee et al. (2007) in a multi-block rupture model.

156 2.4 Northern Sumatra 2005 (SU05)

157 On 28 March 2005, a M_w 8.6 earthquake occurred 160 km to the south of the SU04 epicentre (Figure
158 1) as a result of thrust faulting along the interface of the Australian and Sunda plates (Hayes et al.,
159 2017). The event had a maximum slip of ~12 m along a 360 km by 200 km (length x width) fault
160 patch (Banerjee et al., 2007). This earthquake is likely to have been the result of stress changes
161 following the SU04 event (Hayes et al., 2017).

162 2.5 Southern Sumatra 2007 (SU07)

163 The M_w 8.5 event on 12 September 2007 occurred along the offshore plate boundary of the
164 Australian and Sunda plates as a result of shallow thrust faulting (Hayes et al., 2017). Twelve hours
165 later a M_w 7.9 event followed in the same area with similar mechanism. Maximum slip of ~8 m was
166 modelled on a fault patch of 250 km by 170 km (length x width) (Konca et al., 2008) for the
167 combined event. These events occurred further south east along the Australian and Sunda plate
168 boundary, closer to the Australian mainland compared to the other Sumatran events considered in
169 Figure 1 and are considered in a combined fault model.

170 2.6 Northern Sumatra 2012 (SU12)

171 Two large strike-slip intraplate earthquakes, separated by 200 km, occurred as a sequence on 11
172 April 2012 with moment magnitudes M_w 8.6 and 8.2 in the oceanic lithosphere of the Cocos Basin
173 (Duputel et al., 2012). The location is represented as a single event (SU12) in Figure 1. The initial
174 M_w 8.6 mainshock represents a complex four-fault structure with large slip (20-30 m) (Yue et al.,
175 2012). Focal mechanism solutions are consistent in indicating that each of these events could have
176 occurred as the result of left-lateral slip on a north-northeast striking fault or right-lateral slip on a
177 west-northwest-striking fault (Hayes et al., 2017), and are considered here as a combined fault
178 model.

179 2.7 Australian intraplate earthquakes

180 The seismic cycle and strain rates provide important information regarding the implications for
181 intraplate seismicity and stresses (Trubienko et al., 2013). Although the occurrence of 'moderate-
182 large' ($>M_w$ 5.0) earthquakes is infrequent in Australia, there is still a record of events that have
183 caused surface ruptures, listed in Table 2. Geodetic studies are not available for most of these events
184 (many of which predate the GPS). Although they have been studied using seismology, their small size
185 and remote location with respect to Australian population centres means they are not always well
186 observed.

187 The data used to infer neotectonic structures presented in Clark et al. (2014) suggests that the
188 primary cause for ongoing deformation of the Indo-Australian plate is an active response to distant
189 plate boundary interactions. With ongoing changes at the plate margins, the Australian continent
190 will continue to deform at some level in response to plate boundary forces (Hillis et al., 2008,
191 Sandiford et al., 2004, Tregoning et al., 2013), also with series of intraplate events occurring in
192 specified seismic zones (e.g. Dentith and Featherstone, 2003, Revets et al., 2009, Sandiford and
193 Egholm, 2008). An understanding of the plate boundary events is therefore critical for interpreting
194 transient present-day surface deformation as observed by GPS. We now investigate these events
195 using the geodetic record as well as co- and postseismic modelling with a simplistic one-dimensional
196 earth structure to assess ongoing deformation.

197 3 Data & Methods

198 3.1 GPS time series

199 Following the methods outlined in Riddell et al. (2020), the GPS data over the period 2000.0-2019.0
200 was sourced from the Geoscience Australia GNSS data archive (<https://gnss.ga.gov.au/>), and daily
201 point positions were estimated using GIPSY v6.3 software with clock and orbit products (repro2)
202 from the Jet Propulsion Laboratory (JPL) (Bertiger et al., 2010, Zumberge et al., 1997). Further details

203 describing the processing, including outlier and offset detection and removal is described in Riddell
204 et al. (2020). The daily GPS series were aligned to ITRF2014 (Altamimi et al., 2016).

205 Elastic deformations due to atmospheric loading were removed from the time series using the
206 Modern-Era Retrospective analysis for Research and Applications, Version 2 (MERRA2) gridded
207 products (Gelaro et al., 2017), as well as deformations due to terrestrial land water storage,
208 computed using land water storage pressure from the numerical weather model MERRA2 (Reichle et
209 al., 2017), and non-tidal ocean loading from ocean bottom pressure fields of the Max-Planck-
210 Institute for Meteorology Ocean Model (MPIOM; Jungclaus et al., 2013). These estimates of elastic
211 deformation were downloaded from the International Mass Loading Service (Petrov, 2015) in the CF
212 frame (Blewitt, 2003), which is appropriate for correcting non-secular changes in coordinate time
213 series in the ITRF (Dong et al., 2003). We note that the earlier segments of the GPS time series (prior
214 to 2005) are especially sensitive to receiver changes. Offsets due to equipment and firmware
215 changes are estimated and removed simultaneously with a linear and seasonal (solar annual and
216 semi-annual) model. The estimated offset times and magnitudes are provided in the Supporting
217 Information (Table S2).

218 3.2 Coseismic modelling

219 The expected elastic coseismic deformation for each earthquake is computed on a spherically
220 layered Earth with STATIC1D (Pollitz, 1996). An Earth model with 69 layers defined by the
221 Preliminary Earth Reference Model (PREM) (Dziewonski and Anderson, 1981) was used with a
222 maximum spherical harmonic degree of 1500, sufficient to resolve deformation with a spatial scale
223 of approximately 13 km. Regions radially deeper than 3300 km were considered as an
224 incompressible fluid and the ocean in PREM was replaced by crust. Fault slip parameters from the
225 references given in Table 1 are used to derive estimates of coseismic slip.

226 Modelled coseismic slip displacements were compared to coseismic offsets (in 3D) computed using
227 daily GPS data. The instantaneous coseismic offset magnitude is calculated using two weeks of GPS

228 data either side of the time of the earthquake, fitting a linear trend with a Heaviside jump using
229 ordinary least squares. Recognizing that white noise dominates over short periods in GPS time series
230 we take the formal uncertainties to represent the offset uncertainty. We use two weeks of data to
231 calculate the coseismic offset magnitude as a compromise between biases caused by postseismic
232 relaxation, daily variability and noise correlation (e.g., King and Santamaría-Gómez, 2016, Watson et
233 al., 2010). Similar results are found with estimating the coseismic offset using only one week either
234 side of the event. Where the modelled coseismic displacements disagree with the computed offsets,
235 we scale the slip model accordingly by adopting the modified result that retains agreement with the
236 seismic location and fault geometry of the event, while most closely fitting the GPS (e.g. Jiang et al.,
237 2018, King and Santamaría-Gómez, 2016). An arbitrary value of 1.5 for the weighted root mean
238 square (WRMS) is chosen as acceptable. The site selection for constraining the coseismic model was
239 based on data availability, data quality and distance from the earthquake epicentre.

240 3.3 Postseismic modelling

241 Near-field deformation after an earthquake is a response to the combination of coseismic
242 displacement followed by viscoelastic relaxation and fault after-slip which can be difficult to separate
243 (Bedford et al., 2016, Wang et al., 2012). Afterslip is motion at depth along the fault face causing
244 local deformation, approximately within 200 km of the earthquake epicentre (Klein et al., 2016,
245 Wang et al., 2012). We assume that far-field deformation does not contain a signal from after-slip,
246 given most of our GPS locations are more than 500 km from the earthquake epicentres. We
247 therefore only model viscoelastic postseismic processes.

248 We make use of the VISCO1D (Pollitz, 1992, 1997) code to compute the viscoelastic deformation
249 with a linear bi-viscous (Burgers) rheology. VISCO1D computes surface displacements generated by
250 an earthquake using a symmetric spherically layered elastic-viscoelastic Earth model. The surface
251 displacements are controlled by fault parameters (latitude and longitude of lower fault corner,
252 strike, rake, dip, slip, length, and the depth of the upper and lower fault edges); as well as the

253 relative thicknesses and rheological properties of the chosen layers. Following King and Santamaría-
254 Gómez (2016), multiple versions of the model were run with varying thickness of an elastic
255 lithosphere ranging from 30-130 km, asthenosphere thickness and effective viscosity (0-190 km;
256 1×10^{17} - 5×10^{21} Pa s), and upper mantle thickness and effective viscosity (320-670 km; 2×10^{18} - 5×10^{21} Pa
257 s). Predictions from VISCO1D can be sensitive the layers of the lower mantle (Grace Nield, pers.
258 comm. February 2020). We include a lower mantle with 30 layers with bulk and shear modulus
259 values of 44×10^{10} Pa and 22×10^{10} Pa respectively. This difference in handling the lower mantle did
260 produce different results to those without a detailed lower mantle such as were published by
261 Tregoning et al. (2013). An example earth model (readable by VISCO1D v3) is provided in the
262 Supporting Information (File S1). The values of density, bulk modulus and shear modulus were taken
263 from PREM and depth-averaged for each layer in our model. Gravity was taken into consideration
264 during the computations.

265 We use GPS daily time series to assess the predicted surface deformation from VISCO1D and select
266 the best fit model based on the chi-square per degree of freedom statistic and the lowest value of
267 the standard deviation from an ordinary least squares fit. The best fit model is chosen independently
268 for the horizontal (east and north combined) and vertical components per site.

269 4 Results

270 Here we present results of the computed coseismic offsets for the earthquakes in Table 1, followed
271 by the postseismic deformation. The Sumatran events that occurred in 2004, 2005, 2007 and 2012
272 are presented as a compilation of observed and modelled deformation, whereas all other events are
273 presented singularly.

274 4.1 Macquarie Ridge 2004 (MI04)

275 4.1.1 Coseismic displacements

276 Site selection is limited by the availability of GPS data before 2004, with eight far-field sites in
277 southeast Australia with data available from 2000.0 onwards (Table 3). The largest coseismic offset
278 of 5.98 ± 1.33 mm is in the east component of HOB2 (Hobart), which is the closest site on the
279 Australian continent that sits in the far-field of the MI04 event (Figure 1; Table 3). Offsets in the
280 vertical components of sites in southeast mainland Australia range from -3.49 ± 2.42 mm to $1.89 \pm$
281 2.65 mm. The uncertainties for the up-component offsets are large for the majority of sites, where
282 only three of the vertical offsets are significant at one-sigma (Table 3). Both the horizontal and
283 vertical offsets are comparable to those calculated by STATIC1D, which provides confidence that the
284 fault geometry parameters taken from Watson et al. (2010) (Table 1) are sufficient and that the
285 model does not require scaling for this study. The WRMS value of the modelled coseismic offsets are
286 comparable to those from Tregoning et al. (2013) and King and Santamaría-Gómez (2016). Our
287 coseismic estimates compare well with those of Watson et al. (2010), with HOB2 being displaced by
288 ~ 5 mm to the east.

289 4.1.2 Postseismic displacement

290 We build on the investigation by Tregoning et al. (2013) of viscoelastic postseismic relaxation
291 occurring after the MI04 earthquake. Our GPS time series adds eight years to those analysed by
292 Tregoning et al. (2013) (end date of 2019.0 compared to 2011.0), we make use of a precise point
293 positioning approach rather than a double differenced solution, and our solutions are aligned to the
294 ITRF2014 reference frame rather than ITRF2008. We also attempt to account for short-term
295 temporal variability by removing surface mass loading caused by atmospheric, hydrologic and non-
296 tidal sources.

297 Figure 2 shows the coordinate time series for three sites in SE Australia over the period 2000.0–
298 2019.0, encompassing the MI04 event. The velocity for the period prior to the earthquake (2000.0–

299 2004.9) was removed from the entire time series to highlight any postseismic change in velocity. The
300 velocity prior-to and following the earthquake are calculated using Hector software (Bos et al.,
301 2013), adopting a power-law plus white (PLW) noise model including estimates of linear, annual and
302 semi-annual terms and coseismic offset. The linear velocity post-earthquake is plotted in Figure 2 as
303 a blue dashed line.

304 The site time series in Figure 2 are shown as they experienced the largest change in velocity
305 following the MI04 event based on our analysis. We have chosen to use TID1 instead of TIDB as the
306 time series is of slightly better quality (smaller scatter and the difference between the time series
307 shows no distinct trends). We distrust the Melbourne (MOBS) time series over this time period as it
308 shows substantially different behaviour compared to the other sites (Figure S1), presumably due to
309 the short pre-MI04 time series making the pre-MI04 velocity unreliable and/or being affected by
310 substantial near-field multipath (Moore et al., 2014). Tregoning et al. (2013) also cover this event
311 and we return to this in the discussion.

312 We compared model predictions from VISCO1D with the time series/velocities for each of the GPS
313 sites. The coloured lines in Figure 2 represent the optimal models where red is the best fitting
314 viscoelastic model for the horizontal components, cyan is the best fitting viscoelastic model for the
315 vertical component, and magenta is the best fitting viscoelastic model that is a compromise between
316 the fit to each component (north, east, up). Table 4 contains the parameters of the viscoelastic
317 models that best fit the GPS results for each of the earthquakes considered in Table 1.

318 4.1.2.1 *Horizontal*

319 Table 5 shows the change in velocity of sites in Australia, noting that the northern sites are likely to
320 also contain a postseismic signal from the SU04 event that occurred 3 days after the MI04 event. The
321 decay function in Hector can be set separately and so we look at the full time series (up to 2019.0)
322 following each event. The changes in velocity of the north and east components for the sites in SE
323 Australia (HOB2, MOBS, TIDB, TID1, STR1, CEDU) following the MI04 earthquake are less than 0.5

324 mm/yr (Table 5) with the exclusion of the site on Macquarie Island (MAC1). Our time series analysis
325 for HOB2 agrees with that of Tregoning et al. (2013) with a reduced northward trend. Figure 3 of
326 Tregoning et al. (2013) shows a southerly postseismic velocity relative to the inter-seismic
327 movement in the north component at TIDB, whereas our series for TID1 show northerly motion (as
328 does our series for TIDB). The difference between our TID1 time series at the TIDB time series of
329 Tregoning et al. (2013) may be explained by changes in equipment hardware and firmware. TIDB and
330 TID1 share the same antenna but have different receivers that have been changed and updated at
331 different times. Our velocity estimates for TIDB and TID1 differ by less than 0.1 mm/yr, which
332 provides confidence in our analysis.

333 4.1.2.2 Vertical

334 From Table 5, the observed change in the vertical component is larger than ± 1 mm/yr for most sites
335 over the period 2004.9 – 2019.0. STR1, TIB1, and HOB2 all show uplift in the 4.5 years prior to the
336 MI04 earthquake, but following the event, the series each shows subsidence over the next 14.5
337 years. The postseismic change in vertical velocity is 1.5-3.5 mm/yr for the sites with a consistent shift
338 towards subsidence after the MI04 earthquake. The largest change in vertical velocity (-3.24 mm/yr)
339 is observed at STR1 where the pre-earthquake velocity changes from 1.97 ± 0.50 mm/yr to $-1.27 \pm$
340 0.21 mm/yr post-earthquake. No postseismic deformation model fits the GPS well in the vertical and
341 we return to this in the discussion.

342 4.2 Sumatran events

343 Given that the Sumatran events cluster closely together in time and space it is not possible to
344 independently analyse postseismic deformation due to each earthquake. Instead, we present the
345 combined results of the events that occurred in northern and southern Sumatra over the period
346 2004 – 2012. Following the previous methodology, the coseismic offsets are calculated with
347 STATIC1D for each earthquake and then compared to the observed offset in the GPS time series.
348 Then the postseismic deformation is modelled for each earthquake individually (SU04, SU05, SU07,

349 SU12), with the total accumulated displacement for each model setup compared to the GPS time
350 series to identify the best-fit viscoelastic postseismic model.

351 4.2.1 Coseismic displacements

352 We show the estimated coseismic displacements in Table 6 at the Australian GPS sites located on
353 islands off the NW shelf, Cocos Island (COCO) and Christmas Island (XMIS), as well as sites on
354 mainland Australia (Figure 1). The only available GPS data in the NW Australian region, following the
355 2004/2005 earthquakes in the Sumatran region, are from COCO and Karratha (KARR, see Table S2
356 and Figure 1). For the modelling of the coseismic displacements of the SU04 event we used the total
357 slip displacement of five sub-sources over ten rupture planes from Banerjee et al. (2007) obtaining
358 an WRMS of 0.62 mm. We also explored using instead a scaled version of the USGS solution but the
359 smallest WRMS derived was 1.13 mm and so we adopted the Banerjee et al. (2007) solution. The
360 large uncertainties on the coseismic offsets are due to noisy time series in the mid-2000's due to
361 receiver tracking and scintillation issues (e.g. Conker et al., 2003), and we return to this in the
362 discussion. Coseismic offsets at the available sites across Australia are shown in Table 6 for each of
363 the Sumatran earthquakes considered.

364 Noting that the northern SU05 event occurred three months after the SU04 event, we modelled the
365 event as a separate solution, and remove the estimated coseismic signal of the SU04 event from the
366 GPS series before modelling the 2005 event. The calculated coseismic offsets for the SU05 event
367 have a WRMS of 0.83 mm when compared to the GPS estimates. The coseismic model is used in the
368 viscoelastic modelling without scaling. For this event we only consider the GPS sites at Darwin
369 (DARW) and KARR to constrain the coseismic model. We do not use COCO time series to constrain
370 the model because we are restricting the constraining sites to mainland Australia. Both sites show
371 offsets in the north component, with the KARR offset greater than 4 mm (Table 6). KARR has a
372 significant offset in the vertical component of -2.71 ± 1.56 mm.

373 For the sequence of events in southern Sumatra in 2007, we calculate the coseismic offsets at
374 Australian sites that have available GPS data, again shown in Table 6. KARR and DARW are again
375 used to constrain the coseismic model. All offsets for KARR in each of the three components are
376 significant, and DARW has significant offsets in the north and up components. The fault rupture
377 models of the two events from Konca et al. (2008) required a small amount of scaling of the slip
378 magnitude for the WRMS value to be acceptable (< 1.5 mm) and for the modelled coseismic
379 displacement to align with the GPS offsets.

380 A simple fault rupture model was adopted to model the far-field deformation associated with the
381 SU12 earthquake. As outlined in Section 2.6, there were two events within 24 hours separated by
382 approximately 200 km. The fault rupture model is that from Yue et al. (2012) with five blocks, the
383 first four blocks are for the earlier M_w 8.6 event and the fifth block for the M_w 8.2 event that
384 occurred 12 hours later. DARW and KARR are used to constrain the slip, without scaling and a
385 resulting WRMS of 1.48 mm. The coseismic offsets at sites on the Australian plate, associated with
386 the SU12 earthquake are given in Table 6. Most sites on mainland Australia, aside from DARW, show
387 significant offsets in the north and up components.

388 4.2.2 Sumatran postseismic displacements

389 We plot the GPS time series and modelled viscoelastic postseismic deformation of the Sumatran
390 events in Figure 3. All four events are combined in an attempt to understand the long-term
391 cumulative effects of postseismic deformation from multiple events that have occurred in the same
392 region. The time series in Figure 3 is detrended relative to the pre-SU04 rate. The GPS velocities for
393 the period prior to 2004, and the Sumatran earthquakes considered here are in Table S4.

394 Only three GPS sites on the Australian mainland have robust data available from 2000 onwards to
395 enable the investigation of postseismic deformation following the SU04 event (Figure 3). We focus
396 on those sites mainland Australia that are closest to the Sumatran events (and have available data),
397 KARR, YAR2 and DARW. Even though these sites are located in the very far-field of the earthquake

398 deformation field, changes in velocity at KARR, YAR2 and DARW are visible as a subsidence signal in
399 Figure 3 (values in Table 7); we take these sites as being representative of the motion across NW
400 Australia. The optimal model for all components is represented by a magenta line in Figure 3 where
401 the solid line is the modelled postseismic deformation for SU04 only and the dashed line is the
402 cumulative deformation from each of the four Sumatran events. Other than SU04, the remaining
403 events have a subtle effect on the observed long-term deformation at each site (dashed line in
404 Figure 3).

405 4.2.2.1 *Horizontal*

406 The changes in velocity following the SU04 event are shown in Table 7 for each of the Australian GPS
407 sites that have data from 2000 onwards to ensure that we capture the full extent of the cumulative
408 postseismic displacement from each of the four Sumatran events across the Australian continent.
409 The observed postseismic deformation of the east component is well matched by the modelled
410 viscoelastic relaxation for each of the sites in Table 7, and the observed deformation in the northern
411 components is well represented at YAR2 and DARW, but not at KARR. The time series at KARR is
412 subject to many hardware changes in the early part of the series which introduces uncertainty in the
413 velocity estimation, suggesting that the change in trend pre- and post-earthquake could be
414 unrealistic, with large uncertainty.

415 4.2.2.2 *Vertical*

416 The velocity changes in the vertical component following the Sumatran events are in Table 7 for
417 each of the Australian GPS. The dominant change in velocity is subsidence following the SU04 event
418 with the sites in NW Australia showing a change in trend for the vertical component ranging
419 between -2 to -2.5 mm/yr (Table 7), which is also visible in Figure 3. The observed postseismic
420 deformation at KARR and YAR2 is well modelled by the viscoelastic response, whereas DARW is not.
421 The DARW postseismic model suggests a gradual return to pre-SU04 trend which is not replicated by
422 the GPS observations.

423 4.3 Puysegur Trench 2009 (PT09)

424 4.3.1 Coseismic displacements

425 The coseismic offsets estimated at nearby Australian GPS sites due to the 2009 M_w 7.8 Puysegur
426 event are listed in Table 8. Significant offsets are observed in sites for the north and up components
427 for some sites, although the magnitude of the offset does not show a clear linear relationship with
428 distance from the location of the earthquake. This implies that the axis of the lobes of the
429 deformation are oblique to a transect taken from south to north through the sites.

430 The coseismic offsets in the horizontal component are all positive, indicating a shift of the sites
431 north-east, whereas the vertical coseismic offsets are mixed with significant displacements (at one-
432 sigma) at HOB2 with a subsidence of -3.13 ± 2.53 mm, and the remainder of the sites suggesting
433 uplift of 1.54 ± 1.33 mm at MOBS and 3.26 ± 2.30 mm at Tidbinbilla (TID1) (Table 8). Insignificant
434 coseismic offsets in the east component are observed at the majority of GPS sites on the Australian
435 continent as a result of the PT09 event, where the uncertainty of the east component is large
436 (greater than 2 mm) due to noisy time series at this time. The offsets observed in the GPS series for
437 all components are comparable to those calculated with STATIC1D, with a WRMS of 1.17 mm. Out of
438 interest, we also compared the coseismic offsets for several sites in New Zealand with Mahesh et al.
439 (2011) and Beavan et al. (2010), these are detailed in the Supporting Information (Text S1).

440 4.3.2 Postseismic displacement

441 Time series of the Australian GPS sites after the M_w 7.8 Puysegur event are shown in Figure 4, where
442 the estimated pre-earthquake velocity (2006.0-2009.5) is removed from the full time series. There
443 magnitude of the changes does not vary simply with distance from the rupture. The sites are
444 ordered in Figure 4 from north (left) to south (right) and the coloured lines match the previous
445 description of the optimal models for the components and combined results. We note that there is
446 some residual MI04 deformation present in the timeseries, but it is largely linear and hence removed

447 when we subtract pre-earthquake velocity from our time series. The rheological structure of the
448 optimal model for the PT09 event is similar to that for the MI04 optimal model (Table 4).

449 4.3.2.1 *Horizontal*

450 The change in horizontal velocity for HOB2 and MOBS show statistically significant changes in the
451 north component, and SYDN and MOBS showing statistically significant (but opposite) changes in the
452 east velocity (Table 9). There appears to a visible offset at HOB2, TID1 and MOBS in the east
453 component in 2009, but our method does not see it as significant due to high frequency noise. In
454 Figure 4, MOBS show a noticeably high temporal variability over the period 2011-2014 in the north
455 component, which remains unexplained. The difference may be due to sites in the south east of
456 Australia still undergoing a small amount of postseismic deformation following the MI04 event,
457 which is most significant in the north component (Tregoning et al., 2013, Watson et al., 2010).

458 4.3.2.2 *Vertical*

459 The velocity changes following the PT09 event in Figure 4 show no specific spatial pattern, with the
460 largest change in the vertical component. The HOB2 site shows a velocity change larger than 1
461 mm/yr in the vertical component (Figure 4, Table 9) following the earthquake. The sites at TID1,
462 MOBS and HOB2 demonstrate an increase in the rate of subsidence following the PT09 event (Figure
463 4), but Sydney (SYDN), with a lower latitude, shows positive change in trend.

464 5 Discussion

465 Our observational dataset (2000.0-2019.0) shows that not only has Australia deformed co-
466 seismically and post-seismically in the horizontal component, it has (and continues to) deform in the
467 vertical component since a series of events in 2004. Given the large earthquakes considered here
468 occur close in time to the deployment of much of Australia's geodetic GNSS infrastructure, most
469 Australian coordinate time series are affected by coseismic and postseismic deformation and
470 therefore should not be considered as entirely consistent with longer-term inter-seismic velocities.

471 The period 2000.0-2004.9 represents the longest period in our dataset with GPS data unaffected by
472 significant earthquake activity (i.e., over this period there are no events $> M_w$ 7.5 within subduction
473 zones around the Australian plate boundary). While data exists before 2000 at about 12 sites, we
474 note that the time series up to around the mid-2000s are complicated by frequent equipment
475 changes (both antenna/receiver hardware and firmware) which increases the time series variability
476 and the estimated velocity uncertainties. Nevertheless, we consider these velocities to be our most
477 reliable estimate of the inter-seismic vertical velocity as we take into consideration the most up-to-
478 date PPP processing strategy and models and simultaneously estimate seasonal signals,
479 contributions from surface mass loading and identified offsets from equipment and firmware
480 changes.

481 The inter-seismic velocities for the sites considered in this paper are given in Table 10 (2000.0-
482 2004.9) and demonstrate a range in the vertical component from -3.95 ± 1.59 to 1.76 ± 0.61 mm/yr
483 with an average magnitude and average sigma of -0.52 ± 0.64 mm/yr (excluding island sites COCO
484 and MAC1). The pre-2004 signals are mixed in sign, with sites at Darwin (DARW), Hobart (HOB2),
485 Melbourne (MOBS) and New Norfolk (NNOR) indicating subsidence ranging from -3.95 ± 1.59 to -
486 1.09 ± 0.52 mm/yr. The remaining mainland Australia sites at Ceduna (CEDU), Karratha (KARR), Mt
487 Stromlo (STR1), Tidbinbilla (TID1, TIDB), Townsville (TOW2) demonstrate uplift ranging from $0.29 \pm$
488 0.64 to 1.76 ± 0.61 mm/yr. We note that MOBS and NNOR only have data from 2002.8 and 2002.5
489 respectively while PERT is likely undergoing subsidence due to local groundwater extraction (e.g.
490 Featherstone et al., 2012, Featherstone et al., 2015). Note that these rates do not consider the
491 effects of inter-decadal surface mass transport (largely driven by ice mass change) on vertical land
492 motion, which would shift the estimates in Australia by -0.4 mm/yr in a centre of mass frame (Riva et
493 al., 2017), or ~ 0.2 mm/yr in a centre of figure frame. Nor does it consider the potential biases due to
494 errors in reference frame origin (Riddell et al., 2017) or in the scale rate.

495 The series of large earthquakes in the Sumatra region over the period 2004 – 2012 caused significant
496 changes in GPS vertical velocity estimates at Australian island territories and surface deformation at
497 sites on the Australian mainland. Cocos (COCO) and Christmas Island (XMIS) are located on small
498 islands in the Indian Ocean, whereas Karratha (KARR) and Broome (BRO1) are on the Australian
499 mainland (Figure 1). Distant sites from the Sumatran events, such as Darwin, observe postseismic
500 deformation in the horizontal and vertical components ongoing to at least 2010. Large subsidence
501 (up to 4 mm/yr) is evident, particularly due to the 2004 Sumatran event, and observable
502 deformation is seen to extend as far south as Karratha (KARR, 3500 km) and as far east as Darwin
503 (DARW, 4200 km). While the changes in velocities, in all three components, are smaller following
504 the SU12 earthquake, they are still evident in the time series at these very distant sites.

505 We find coseismic displacements of up to 3 mm at distances more than 5000 km from the
506 earthquake event, highlighting that coseismic deformation can be far reaching across the Australian
507 continent. For the Sumatran events (Table 6) we find the largest coseismic displacement in the
508 vertical component after SU05 of -5.63 ± 2.63 mm at Yarragadee (YAR2), 3890 km from the event.
509 The coseismic displacements for the MI04 event are shown in Table 3 and range, over distances of
510 up to 3000 km, from insignificantly different from zero to 4.01 ± 0.99 mm in the northern
511 component, up to 5.98 ± 1.33 mm in the eastern component and -3.49 ± 2.42 mm to 2.80 ± 1.86 mm
512 in the vertical component. At the time of the PT09 event, we find coseismic displacements (Table 8)
513 that reach 2.73 ± 0.79 mm in the northern component, 3.89 ± 5.00 mm in the eastern component
514 (noting the large uncertainty) and -3.13 ± 2.53 mm to 3.26 ± 2.30 mm in the vertical component over
515 distances of up to 2000 km. The coseismic estimates that are statistically significant (one-sigma) are
516 highlighted in each of the tables using bold text, and we note an increased uncertainty on the
517 vertical estimates.

518 Our preferred viscoelastic Earth model for MI04 is different to that identified by Tregoning et al.
519 (2013). There are a several reasons that are likely to contribute to this. First, our time series are

520 computed differently to those used by Tregoning et al. (2013), although our modelling approach is
521 broadly similar. In particular, the data period used to estimate the postseismic velocities is 8 years
522 longer than used in Tregoning et al. (2013). Further, To determine if the additional length of the
523 series affected the velocities pre- and post-earthquake, velocities were recomputed for the period
524 2004.9-2011.0 (Table S3), matching the time period in Tregoning et al. (2013). The postseismic
525 velocity estimates for the shorter period showed insignificant differences for the north and east
526 components. The postseismic velocity uncertainties for HOB2, MOBS, STR1 and TID1 from the
527 shorter series are about half that of those from the longer series.

528 Compared to Tregoning et al. (2013), we also use a different earth model as input into VISCO1D. We
529 explicitly model the lower mantle in VISCO1D which made important differences to the model
530 outputs. The template Earth model in VISCO1D is explicitly specified down to 670 km, with the
531 lowest layer representing everything that sits below it. Adding explicit lower mantle layers both
532 changes the predictions and improves agreement with an independent model (Grace Nield, pers.
533 comm. February 2020). In our case, the fit of the viscoelastic models to the post-earthquake GPS
534 velocity estimate was dramatically improved with the addition of an explicit lower mantle.

535 Of the earthquakes considered here, none of the postseismic deformation model predictions
536 reproduce the observations in all three components. Earth models inferred from seismic
537 tomography over Australia and its region provide evidence of substantial lateral variations at
538 different depths (e.g. Debayle et al., 2005, Lekić and Romanowicz, 2011). These variations may be
539 sufficiently large to mean that a 1D rheological model may not be appropriate for modelling post-
540 seismic deformation of Australia and a 3D rheological model could be required to explain the
541 observations. King and Santamaría-Gómez (2016) also suggested this to be the case for postseismic
542 deformation of East Antarctica caused by far field earthquakes occurring in an oceanic setting.

543 In our analysis, we have assumed all deformation beyond ~500 km from the earthquake event is in
544 the far-field and can be attributed to viscoelastic postseismic deformation and not afterslip. The

545 frictional response of the fault interface causes the near-field postseismic deformation to be
546 dominated by afterslip (e.g. Marone, 1998). The implication for assuming no, or minimal,
547 contribution from early afterslip behaviour is that the coseismic estimates can be biased by up to
548 10% (Twardzik et al., 2019). This has a small effect given the limitations of the 1D viscoelastic model.
549 Previously it has been suggested that while horizontal deformations are important for the accuracy
550 of the reference frame in Australia, vertical deformations have a negligible effect (e.g. Tregoning et
551 al., 2013). Our results suggest that this is not correct and failure to consider deformation in the
552 vertical component will have implications for the realization of the terrestrial reference frame. The
553 current realisation of the frame (ITRF2014) does not consider the effects of the earthquakes we
554 study on most Australian sites. Despite the demonstration of postseismic horizontal deformation of
555 continental Australia by Tregoning et al. (2013) (e.g., HOB2, MOBS figure 1), Altamimi et al. (2016)
556 only considered postseismic deformation at COCO and MAC1 (both island sites) during the
557 construction of ITRF2014.

558 In this study we find substantial coseismic and postseismic deformations from several other
559 earthquakes not considered in ITRF2014. For instance, we find significant coseismic offsets also
560 occurred at several Australian sites as a result of the 2009 Puysegur Trench earthquake. This
561 earthquake is not listed as having observable coseismic or postseismic deformation at Australian
562 sites in publicly available offset files, such as those used in the realization of ITRF2014, available at
563 <ftp://ftp.iers.org/products/reference-systems/terrestrial/itrf/itrf2014/ITRF2014-soln-gnss.snx>
564 (Altamimi et al., 2016), or for open access GPS time series, such as those in the Nevada Geodetic
565 Laboratory "steps.txt" file, that is available at <http://geodesy.unr.edu/NGLStationPages/steps.txt>.
566 Blewitt et al. (2018) use a threshold based on the distance of the GPS site from the earthquake to
567 determine if there is possible expected seismic transient deformation at a site. The threshold (r_0) is
568 calculated as a simple function of the earthquake magnitude: $r_0 = 10^{(M_w * 0.5 - 0.8)}$. In this instance the

569 Australian GPS sites are beyond the distance threshold for the M_w 7.8 PT09 earthquake, and so
570 would not be recognized in an automated procedure based purely on distance from the earthquake.

571 In some cases, present-day deformation at GNSS sites is still occurring in response to earthquake
572 events that occurred prior to the commencement of the GNSS instrumental record. In these cases,
573 modelling the event assists to understand the spatial variation in postseismic relaxation that cannot
574 be detected from geodetic time series. We explored the effect of the 1979 M_w 7.8 Puysegur Trench
575 earthquake on the present-day deformation of Australia. The 1979 event was in a similar location to
576 the 2009 event, approximately 110 km separating the two surface epicentres. We considered the
577 ongoing effects of that earthquake using a method similar to that detailed in Watson et al. (2010)
578 where they investigated the deformation of Macquarie Island due to historic earthquakes. Using the
579 range of Earth models adopted in the previous section relating to the Puysegur Trench earthquake in
580 2009, we can predict the surface deformation of the event in 1979 that may cause ongoing surface
581 changes observed at Australian sites. Model outputs suggest that the south east of Australia (HOB2,
582 SYDN, MOBS) may have been still experiencing subsidence of approximately 0.1–0.4 mm/yr during
583 2000.0–2010.0. There is no horizontal deformation (Figure S2) indicated by our modelling over the
584 period 1979–2010. While these deformations are small and maybe considered unreliable given the
585 presence of unmodelled lateral variations in Earth properties, this finding highlights the need to
586 consider postseismic signals from prior to the commencement of the GNSS record, with important
587 impact on our determination of intra-seismic crustal velocities and potentially interpretation of long
588 sea level records from tide gauges.

589 6 Conclusions

590 Using geodetic data, we have identified three dimensional coseismic and postseismic deformation of
591 Australia occurring as a result of several large ($M_w > 7.5$) offshore plate boundary earthquakes since
592 2000. Our work extends the previous identification of horizontal deformation of Australia due to far-

593 field offshore earthquakes by identifying substantial and sustained vertical deformation of Australia.
594 We also study the effects of earthquakes not previously considered.

595 In the vertical component, we find coseismic offsets of up to 3 mm more than 5000 km from the
596 earthquake event, and postseismic signals reaching several mm/yr sustained over several years.
597 While viscoelastic models of postseismic deformation can explain the observed changes in velocity in
598 one or two coordinate components, we were not able to reproduce them in all three coordinate
599 components with a single model. We suggest that this is due to limitations in using viscoelastic
600 deformation models with a 1D (radially varying) Earth model, whereas the Earth rheological
601 structure between the offshore earthquakes and continental Australia is complex.

602 As the demand for an accurate and stable geodetic reference frame increases toward stated
603 international goals, we suggest that the earthquakes discussed here, and the deformation induced in
604 all coordinate components, need to be considered. Given that ITRF2014 did not parameterise
605 postseismic deformation at the sites studied on mainland Australia, there is scope for improvement
606 in future realisations of the frame across this region.

607 There are limitations to this research based on the GPS time series length and the availability of
608 high-quality data, as well as limitations of the 1D viscoelastic modelling that does not consider lateral
609 heterogeneities in rheology. These considerations offer scope for future research to improve
610 observed and modelled postseismic deformation of the Australian continent, and advocates for
611 improvements to available postseismic models. Improvements are required in reducing the number
612 of offsets in time series due to, for example, equipment changes at GNSS sites. Although these are
613 documented and can be applied as an offset in time series analysis, the introduction of offsets
614 weakens the velocity and coseismic estimates at these sites, and potentially changes the noise
615 characteristics (Williams, 2003).

616 Although the effect of vertical land motion due to coseismic and postseismic deformation in
617 Australia is small, it will influence estimates of absolute sea level from tide gauges along the

618 Australian coast. Conversely, the use of satellite altimetry to derive estimates of relative sea level
619 change also requires understanding of vertical land motion. This also has direct relevance to those in
620 the altimetry community who seek to understand systematic error in altimeter records through
621 comparison of altimetry and tide gauges corrected for land motion (e.g. Watson et al. 2015). This
622 work underscores the inadequacy of assumptions of linear land motion, even in regions previously
623 thought to be relatively immune from anthropogenic influences on crustal displacement.

624

625 Acknowledgements

626 ARR is a recipient of scholarship funding from Geoscience Australia. The GPS data is available via the
627 Geoscience Australia GNSS Network Portal <https://gnss.ga.gov.au/>. The software for modelling
628 elastic and viscoelastic deformation (STATIC1D and VISCO1D) are available from
629 <https://earthquake.usgs.gov/research/software/>. Some of the figures presented here were created
630 with Generic Mapping Tool (GMT, Wessel et al., 2013).

631 ARR was the primary author who developed the idea, carried out its execution and analysis, and was
632 responsible for the manuscript preparation. MAK and CSW motivated and assisted in the design of
633 the study, contributed to the interpretation and critically revised the manuscript.

634 References

- 635 Altamimi, Z., Rebischung, P., Métivier, L. & Collilieux, X. 2016. ITRF2014: A new release of the
636 International Terrestrial Reference Frame modeling non-linear station motions. *Journal of*
637 *Geophysical Research: Solid Earth*, 121, 6109-6131,doi: 10.1002/2016JB013098.
- 638 Anderson, H., Webb, T. & Jackson, J. 1993. Focal mechanisms of large earthquakes in the South
639 Island of New Zealand: implications for the accommodation of Pacific-Australia plate motion.
640 *Geophysical Journal International*, 115, 1032-1054,doi: 10.1111/j.1365-
641 246X.1993.tb01508.x.

642 Banerjee, P., Pollitz, F., Nagarajan, B. & BÜRgmann, R. 2007. Coseismic Slip Distributions of the 26
643 December 2004 Sumatra–Andaman and 28 March 2005 Nias Earthquakes from gps Static
644 Offsets. *Bulletin of the Seismological Society of America*, 97, S86-S102,doi:
645 10.1785/0120050609.

646 Beavan, J., Samsonov, S., Denys, P., Sutherland, R., Palmer, N. & Denham, M. 2010. Oblique slip on
647 the Puysegur subduction interface in the 2009 July MW 7.8 Dusky Sound earthquake from
648 GPS and InSAR observations: implications for the tectonics of southwestern New Zealand.
649 *Geophysical Journal International*, 183, 1265-1286,doi: 10.1111/j.1365-246X.2010.04798.x.

650 Bedford, J. & Bevis, M. 2018. Greedy Automatic Signal Decomposition and its application to daily GPS
651 time series. *Journal of Geophysical Research: Solid Earth*, 0,doi: 10.1029/2017JB014765.

652 Bedford, J., Moreno, M., Li, S., Oncken, O., Baez, J. C., Bevis, M., Heidbach, O. & Lange, D. 2016.
653 Separating rapid relocking, afterslip, and viscoelastic relaxation: An application of the
654 postseismic straightening method to the Maule 2010 cGPS. *Journal of Geophysical Research:*
655 *Solid Earth*, 121, 7618-7638,doi: 10.1002/2016JB013093.

656 Bertiger, W., Desai, S. D., Haines, B., Harvey, N., Moore, A. W., Owen, S. & Weiss, J. P. 2010. Single
657 receiver phase ambiguity resolution with GPS data. *Journal of Geodesy*, 84, 327-337,doi:
658 10.1007/s00190-010-0371-9.

659 Bevis, M., Taylor, F. W., Schutz, B. E., Recy, J., Isacks, B. L., Helu, S., Singh, R., Kendrick, E., Stowell, J.,
660 Taylor, B. & Calmantli, S. 1995. Geodetic observations of very rapid convergence and back-
661 arc extension at the Tonga arc. *Nature*, 374, 249,doi: 10.1038/374249a0.

662 Bird, P. 2003. An updated digital model of plate boundaries. *Geochemistry, Geophysics, Geosystems*,
663 4,doi: 10.1029/2001GC000252.

664 Blewitt, G. 2003. Self-consistency in reference frames, geocenter definition, and surface loading of
665 the solid Earth. *Journal of Geophysical Research: Solid Earth*, 108,doi:
666 10.1029/2002JB002082.

667 Blewitt, G. Terrestrial Reference Frame Requirements for Studies of Geodynamics and Climate
668 Change. In: VAN DAM, T., ed. REFAG 2014. International Association of Geodesy Symposia,
669 vol 146, 2015 Cham. Springer International Publishing, 209-216.

670 Blewitt, G., Hammond, W. C. & Kreemer, C. 2018. Harnessing the GPS explosion for interdisciplinary
671 science. *Eos, Transactions American Geophysical Union*, 99,doi:
672 <https://doi.org/10.1029/2018EO104623>.

673 Bock, Y. & Melgar, D. 2016. Physical applications of GPS geodesy: a review. *Reports on Progress in*
674 *Physics*, 79, 106801,doi: 10.1088/0034-4885/79/10/106801.

675 Bos, M. S., Fernandes, R. M. S., Williams, S. D. P. & Bastos, L. 2013. Fast error analysis of continuous
676 GNSS observations with missing data. *Journal of Geodesy*, 87, 351-360,doi: 10.1007/s00190-
677 012-0605-0.

678 Bowman, J. R., Gibson, G. & Jones, T. 1990. Aftershocks of the 1988 January 22 Tennant Creek,
679 Australia Intraplate Earthquakes: Evidence for a Complex Thrust-Fault Geometry.
680 *Geophysical Journal International*, 100, 87-97,doi: 10.1111/j.1365-246X.1990.tb04570.x.

681 Burbidge, D. R. 2004. Thin plate neotectonic models of the Australian plate. *Journal of Geophysical*
682 *Research: Solid Earth*, 109,doi: 10.1029/2004jb003156.

683 Burgette, R. J., Watson, C. S., Church, J. A., White, N., J., Tregoning, P. & Coleman, R. 2013.
684 Characterising and minimising the effects of noise in tide gauge time series: relative and
685 geocentric sea level rise around Australia. *Geophys. J. Int.*, 194, 719-736,doi:
686 10.1093/gji/ggt131.

687 Clark, D., Mcpherson, A. & Allen, T. 2014. Intraplate earthquakes in Australia. In: TALWANI, P. (ed.)
688 *Intraplate Earthquakes*. Cambridge: Cambridge University Press.

689 Conker, R. S., El-Arini, M. B., Hegarty, C. J. & Hsiao, T. 2003. Modeling the effects of ionospheric
690 scintillation on GPS/Satellite-Based Augmentation System availability. *Radio Science*, 38, 1-1-
691 1-23,doi: 10.1029/2000rs002604.

692 Crone, A. J., Machette, M. N. & Bowman, J. R. 1992. Geologica investigations of the 1988 Tennant
693 Creek, Australia, earthquakes; implications for paleoseismicity in stable continental regions.
694 United States Geological Survey Bulletin 2032-A.

695 Crone, A. J., Machette, M. N. & Bowman, J. R. 1997. Episodic nature of earthquake activity in stable
696 continental regions revealed by palaeoseismicity studies of Australian and North American
697 quaternary faults. *Australian Journal of Earth Sciences*, 44, 203-214,doi:
698 10.1080/08120099708728304.

699 Denham, D., Alexander, L. G., Everingham, I. B., Gregson, P. J., Mccaffrey, R. & Enever, J. R. 1987. The
700 1979 Cadoux earthquake and intraplate stress in Western Australia. *Australian Journal of*
701 *Earth Sciences*, 34, 507-521,doi: 10.1080/08120098708729429.

702 Dentith, M. C. & Featherstone, W. E. 2003. Controls on intra-plate seismicity in southwestern
703 Australia. *Tectonophysics*, 376, 167-184,doi: <https://doi.org/10.1016/j.tecto.2003.10.002>.

704 Dong, D., Yunck, T. & Heflin, M. 2003. Origin of the International Terrestrial Reference Frame.
705 *Journal of Geophysical Research: Solid Earth*, 108,doi: 10.1029/2002JB002035.

706 Duputel, Z., Kanamori, H., Tsai, V. C., Rivera, L., Meng, L., Ampuero, J.-P. & Stock, J. M. 2012. The
707 2012 Sumatra great earthquake sequence. *Earth and Planetary Science Letters*, 351, 247-
708 257,doi: <http://dx.doi.org/10.1016/j.epsl.2012.07.017>.

709 Dziewonski, A. M. & Anderson, D. L. 1981. Preliminary reference Earth model. *Physics of the Earth*
710 *and Planetary Interiors*, 25, 297-356,doi: [http://dx.doi.org/10.1016/0031-9201\(81\)90046-7](http://dx.doi.org/10.1016/0031-9201(81)90046-7).

711 Featherstone, W., Filmer, M. S., Penna, N. T., Morgan, L. M. & Schenk, A. 2012. Anthropogenic land
712 subsidence in the Perth Basin: challenges for its retrospective geodetic detection. *Journal of*
713 *the Royal Society of Western Australia*, 95, 53-62,doi:

714 Featherstone, W. E., Penna, N. T., Filmer, M. S. & Williams, S. D. P. 2015. Nonlinear subsidence at
715 Fremantle, a long-recording tide gauge in the Southern Hemisphere. *Journal of Geophysical*
716 *Research: Oceans*, 120, 7004-7014,doi: 10.1002/2015jc011295.

717 Gelaro, R., Mccarty, W., Suárez, M. J., Todling, R., Molod, A., Takacs, L., Randles, C. A., Darmenov, A.,
718 Bosilovich, M. G., Reichle, R., Wargan, K., Coy, L., Cullather, R., Draper, C., Akella, S., Buchard,
719 V., Conaty, A., Silva, A. M. D., Gu, W., Kim, G.-K., Koster, R., Lucchesi, R., Merkova, D.,
720 Nielsen, J. E., Partyka, G., Pawson, S., Putman, W., Rienecker, M., Schubert, S. D.,
721 Sienkiewicz, M. & Zhao, B. 2017. The Modern-Era Retrospective Analysis for Research and
722 Applications, Version 2 (MERRA-2). *Journal of Climate*, 30, 5419-5454,doi: 10.1175/jcli-d-16-
723 0758.1.

724 Gordon, F. R. & Lewis, J. D. 1980. The Meckering and Calingiri earthquakes October 1968 and March
725 1970. *Western Australia Geological Survey, Bulletin*.

726 Gross, R., Beutler, G. & Plag, H.-P. 2009. Integrated scientific and societal user requirements and
727 functional specifications for the GGOS. In: PLAG, H.-P. & PEARLMAN, M. (eds.) *Global*
728 *Geodetic Observing System: Meeting the Requirements of a Global Society on a Changing*
729 *Planet in 2020*. Berlin, Heidelberg: Springer Berlin Heidelberg.

730 Hayes, G. P., Furlong, K. P. & Ammon, C. J. 2009. Intraplate deformation adjacent to the Macquarie
731 Ridge south of New Zealand—The tectonic evolution of a complex plate boundary.
732 *Tectonophysics*, 463, 1-14,doi: <http://dx.doi.org/10.1016/j.tecto.2008.09.024>.

733 Hayes, G. P., Meyers, E. K., Dewey, J. W., Briggs, R. W., Earle, P. S., Benz, H. M., Smoczyk, G. M.,
734 Flamme, H. E., Barnhart, W. D., Gold, R. D. & Furlong, K. P. 2017. Tectonic summaries of
735 magnitude 7 and greater earthquakes from 2000 to 2015. *Open-File Report*. Reston, VA.

736 Hearn, E. H. 2003. What can GPS data tell us about the dynamics of post-seismic deformation?
737 *Geophysical Journal International*, 155, 753-777,doi: 10.1111/j.1365-246X.2003.02030.x.

738 Hearn, E. H., Pollitz, F. F., Thatcher, W. R. & Onishi, C. T. 2013. How do “ghost transients” from past
739 earthquakes affect GPS slip rate estimates on southern California faults? *Geochemistry,*
740 *Geophysics, Geosystems*, 14, 828-838,doi: 10.1002/ggge.20080.

741 Heine, C., Müller, R. D., Steinberger, B. & Dicaprio, L. 2010. Integrating deep Earth dynamics in
742 paleogeographic reconstructions of Australia. *Tectonophysics*, 483, 135-150,doi:
743 <https://doi.org/10.1016/j.tecto.2009.08.028>.

744 Hejrani, B. & Tkalčić, H. 2019. The 20 May 2016 Petermann Ranges earthquake: centroid location,
745 magnitude and focal mechanism from full waveform modelling. *Australian Journal of Earth
746 Sciences*, 66, 37-45,doi: 10.1080/08120099.2018.1525783.

747 Hillis, R. R., Sandiford, M., Reynolds, S. D. & Quigley, M. C. 2008. Present-day stresses, seismicity and
748 Neogene-to-Recent tectonics of Australia's 'passive' margins: intraplate deformation
749 controlled by plate boundary forces. In: JOHNSON, H., DORÉ, T. G., GATLIFF, R. W.,
750 HOLDSWORTH, R. W., LUNDIN, E. R. & RITCHIE, J. D. (eds.) *The Nature and Origin of
751 Compression in Passive Margins*. Geological Society of London.

752 Jiang, Z., Huang, D., Yuan, L., Hassan, A., Zhang, L. & Yang, Z. 2018. Coseismic and postseismic
753 deformation associated with the 2016 Mw 7.8 Kaikoura earthquake, New Zealand: fault
754 movement investigation and seismic hazard analysis. *Earth, Planets and Space*, 70, 62,doi:
755 10.1186/s40623-018-0827-3.

756 Jungclaus, J. H., Fischer, N., Haak, H., Lohmann, K., Marotzke, J., Matei, D., Mikolajewicz, U., Notz, D.
757 & Von Storch, J. S. 2013. Characteristics of the ocean simulations in the Max Planck Institute
758 Ocean Model (MPIOM) the ocean component of the MPI-Earth system model. *Journal of
759 Advances in Modeling Earth Systems*, 5, 422-446,doi: 10.1002/jame.20023.

760 Keep, M. & Schellart, W. P. 2012. Introduction to the thematic issue on the evolution and dynamics
761 of the Indo-Australian plate. *Australian Journal of Earth Sciences*, 59, 807-808,doi:
762 10.1080/08120099.2012.708360.

763 Kennett, B. L. N. & Blewett, R., S. 2012. Lithospheric Framework of Australia. *Episodes*, 35, 9-22,doi:
764 King, M. A., Keshin, M., Whitehouse, P. L., Thomas, I. D., Milne, G. & Riva, R. E. M. 2012. Regional
765 biases in absolute sea-level estimates from tide gauge data due to residual unmodeled
766 vertical land movement. *Geophysical Research Letters*, 39,doi: 10.1029/2012GL052348.

767 King, M. A. & Santamaría-Gómez, A. 2016. Ongoing deformation of Antarctica following recent Great
768 Earthquakes. *Geophysical Research Letters*, 43, 5,doi: 10.1002/2016GL067773.

769 Klein, E., Fleitout, L., Vigny, C. & Garaud, J. D. 2016. Afterslip and viscoelastic relaxation model
770 inferred from the large-scale post-seismic deformation following the 2010 Mw 8.8 Maule
771 earthquake (Chile). *Geophysical Journal International*, 205, 1455-1472,doi:
772 10.1093/gji/ggw086.

773 Konca, A. O., Avouac, J.-P., Sladen, A., Meltzner, A. J., Sieh, K., Fang, P., Li, Z., Galetzka, J., Genrich, J.,
774 Chlieh, M., Natawidjaja, D. H., Bock, Y., Fielding, E. J., Ji, C. & Helmberger, D. V. 2008. Partial
775 rupture of a locked patch of the Sumatra megathrust during the 2007 earthquake sequence.
776 *Nature*, 456, 631,doi: 10.1038/nature07572

777 <https://www.nature.com/articles/nature07572#supplementary-information>.

778 Machette, M. N., Crone, A. J. & Bowman, J. R. 1993. Geologic investigations of the 1986 Marrayat
779 Creek, Australia, earthquake — implications for paleoseismicity in stable continental regions.
780 United States Geological Survey Bulletin 2032-B.

781 Mahesh, P., Kundu, B., Catherine, J. K. & Gahalaut, V. K. 2011. Anatomy of the 2009 Fiordland
782 earthquake (Mw 7.8), South Island, New Zealand. *Geoscience Frontiers*, 2, 17-22,doi:
783 <http://dx.doi.org/10.1016/j.gsf.2010.12.002>.

784 Marone, C. 1998. Laboratory-derived friction laws and their application to seismic faulting. *Annual*
785 *Review of Earth and Planetary Sciences*, 26, 643-696,doi: 10.1146/annurev.earth.26.1.643.

786 Mccue, K., Barlow, B. C., Denham, D., Jones, T., Gibson, G. & Michael-Leiba, M. 1987. Another chip
787 off the old Australian block. *Eos, Transactions American Geophysical Union*, 68, 609-612,doi:
788 10.1029/EO068i026p00609.

789 Mccue, K., Wesson, V. & Gibson, G. 1990. The Newcastle, New South Wales, earthquake of 28
790 December 1989. *BMR Journal of Australian Geology & Geophysics*, 11, 559-568,doi:

791 Métivier, L., Collilieux, X., Lercier, D., Altamimi, Z. & Beauducel, F. 2014. Global coseismic
792 deformations, GNSS time series analysis, and earthquake scaling laws. *Journal of Geophysical*
793 *Research: Solid Earth*, 2014JB011280,doi: 10.1002/2014jb011280.

794 Moore, M., Watson, C., King, M., McClusky, S. & Tregoning, P. 2014. Empirical modelling of site-
795 specific errors in continuous GPS data. *Journal of Geodesy*, 88, 887-900,doi: 10.1007/s00190-
796 014-0729-5.

797 Müller, D. & Seton, M. 2015. Plate Motion. In: HARFF, J., MESCHEDE, M., PETERSEN, S. & THIEDE, J.
798 (eds.) *Encyclopedia of Marine Geosciences*. Netherlands: Springer.

799 Ostanciaux, É., Husson, L., Choblet, G., Robin, C. & Pedoja, K. 2012. Present-day trends of vertical
800 ground motion along the coast lines. *Earth-Science Reviews*, 110, 74-92,doi: [https://doi.org/](https://doi.org/10.1016/j.earscirev.2011.10.004)
801 [10.1016/j.earscirev.2011.10.004](https://doi.org/10.1016/j.earscirev.2011.10.004).

802 Petrov, L. 2015. The International Mass Loading Service.doi: arXiv:1503.00191.

803 Pfeffer, J., Spada, G., Mémin, A., Boy, J. P. & Allemand, P. 2017. Decoding the origins of vertical land
804 motions observed today at coasts. *Geophysical Journal International*, 210, 148-165,doi:
805 10.1093/gji/ggx142.

806 Polcari, M., Albano, M., Atzori, S., Bignami, C. & Stramondo, S. 2018. The Causative Fault of the 2016
807 Mwp 6.1 Petermann Ranges Intraplate Earthquake (Central Australia) Retrieved by C- and L-
808 Band InSAR Data. *Remote Sensing*, 10, 1311,doi:

809 Pollitz, F. F. 1992. Postseismic relaxation theory on the spherical earth. *Bulletin of the Seismological*
810 *Society of America*, 82, 422-453,doi:

811 Pollitz, F. F. 1996. Coseismic Deformation From Earthquake Faulting On A Layered Spherical Earth.
812 *Geophysical Journal International*, 125, 1-14,doi: 10.1111/j.1365-246X.1996.tb06530.x.

813 Pollitz, F. F. 1997. Gravitational viscoelastic postseismic relaxation on a layered spherical Earth.
814 *Journal of Geophysical Research: Solid Earth*, 102, 17921-17941,doi: 10.1029/97JB01277.

815 Revets, S. A., Keep, M. & Kennett, B. L. N. 2009. NW Australian intraplate seismicity and stress
816 regime. *Journal of Geophysical Research: Solid Earth*, 114,doi: 10.1029/2008jb006152.

817 Riddell, A. R., King, M. A. & Watson, C. S. 2020. Present-Day Vertical Land Motion of Australia From
818 GPS Observations and Geophysical Models. *Journal of Geophysical Research: Solid Earth*,
819 125, e2019JB018034,doi: 10.1029/2019jb018034.

820 Riddell, A. R., King, M. A., Watson, C. S., Sun, Y., Riva, R. E. M. & Rietbroek, R. 2017. Uncertainty in
821 geocenter estimates in the context of ITRF2014. *Journal of Geophysical Research: Solid*
822 *Earth*, 122, 4020-4032,doi: 10.1002/2016JB013698.

823 Riva, R. E. M., Frederikse, T., King, M. A., Marzeion, B. & Van Den Broeke, M. R. 2017. Brief
824 communication: The global signature of post-1900 land ice wastage on vertical land motion.
825 *The Cryosphere*, 11, 1327-1332,doi: 10.5194/tc-11-1327-2017.

826 Sandiford, M. 2007. The tilting continent: A new constraint on the dynamic topographic field from
827 Australia. *Earth and Planetary Science Letters*, 261, 152-163,doi:
828 <https://doi.org/10.1016/j.epsl.2007.06.023>.

829 Sandiford, M. & Egholm, D. L. 2008. Enhanced intraplate seismicity along continental margins: Some
830 causes and consequences. *Tectonophysics*, 457, 197-208,doi:
831 <https://doi.org/10.1016/j.tecto.2008.06.004>.

832 Sandiford, M., Malcolm, W. & David, C. 2004. Origin of the in situ stress field in south-eastern
833 Australia. *Basin Research*, 16, 325-338,doi: 10.1111/j.1365-2117.2004.00235.x.

834 Santamaría-Gómez, A., Gravelle, M., Collilieux, X., Guichard, M., Míguez, B. M., Tiphaneau, P. &
835 Wöppelmann, G. 2012. Mitigating the effects of vertical land motion in tide gauge records
836 using a state-of-the-art GPS velocity field. *Global and Planetary Change*, 98–99, 6-17,doi:
837 <http://dx.doi.org/10.1016/j.gloplacha.2012.07.007>.

838 Schumacher, M., King, M. A., Rougier, J., Sha, Z., Khan, S. A. & Bamber, J. L. 2018. A new global GPS
839 data set for testing and improving modelled GIA uplift rates. *Geophysical Journal*
840 *International*, 214, 2164-2176,doi: 10.1093/gji/ggy235.

841 Thom, A. 2017. Australian Earthquakes 2016. *Australian Earthquake Engineering Society 2017*
842 *Conference*. Canberra.

843 Tregoning, P., Burgette, R., McClusky, S. C., Lejeune, S., Watson, C. S. & McQueen, H. 2013. A decade
844 of horizontal deformation from great earthquakes. *Journal of Geophysical Research: Solid*
845 *Earth*, 118, 2371-2381,doi: 10.1002/jgrb.50154.

846 Trubienko, O., Fleitout, L., Garaud, J.-D. & Vigny, C. 2013. Interpretation of interseismic deformations
847 and the seismic cycle associated with large subduction earthquakes. *Tectonophysics*, 589,
848 126-141,doi: <http://dx.doi.org/10.1016/j.tecto.2012.12.027>.

849 Trubienko, O., Garaud, J. D. & Fleitout, L. 2014. Models of postseismic deformation after
850 megathrust earthquakes: the role of various rheological and geometrical parameters of the
851 subduction zone. *Solid Earth Discuss.*, 2014, 427-466,doi: 10.5194/sed-6-427-2014.

852 Twardzik, C., Vergnolle, M., Sladen, A. & Avallone, A. 2019. Unravelling the contribution of early
853 postseismic deformation using sub-daily GNSS positioning. *Scientific Reports*, 9, 1775,doi:
854 10.1038/s41598-019-39038-z.

855 Walwer, D., Calais, E. & Ghil, M. 2016. Data-adaptive detection of transient deformation in geodetic
856 networks. *Journal of Geophysical Research: Solid Earth*, 121, 2129-2152,doi:
857 10.1002/2015JB012424.

858 Wang, K., Hu, Y. & He, J. 2012. Deformation cycles of subduction earthquakes in a viscoelastic Earth.
859 *Nature*, 484, 327-332,doi:

860 Watson, C., Burgette, R., Tregoning, P., White, N., Hunter, J., Coleman, R., Handsworth, R. & Broisma,
861 H. 2010. Twentieth century constraints on sea level change and earthquake deformation at
862 Macquarie Island. *Geophysical Journal International*, 182, 781-796,doi: 10.1111/j.1365-
863 246X.2010.04640.x.

864 Webb, T. H. & Lowry, M. A. 1982. The Puysegur Bank earthquake of 1979 October 12. *New Zealand*
865 *Journal of Geology and Geophysics*, 25, 383-395,doi: 10.1080/00288306.1982.10421505.

866 Wessel, P., Smith, W. H. F., Scharroo, R., Luis, J. & Wobbe, F. 2013. Generic Mapping Tools: Improved
867 Version Released. *Eos, Transactions American Geophysical Union*, 94, 409-410,doi:
868 10.1002/2013eo450001.

869 Williams, S. D. P. 2003. Offsets in Global Positioning System time series. *Journal of Geophysical*
870 *Research: Solid Earth*, 108,doi: 10.1029/2002JB002156.

871 Yue, H., Lay, T. & Koper, K. D. 2012. En echelon and orthogonal fault ruptures of the 11 April 2012
872 great intraplate earthquakes. *Nature*, 490, 245-249,doi: 10.1038/nature11492.

873 Zumberge, J. F., Heflin, M. B., Jefferson, D. C., Watkins, M. M. & Webb, F. H. 1997. Precise point
874 positioning for the efficient and robust analysis of GPS data from large networks. *Journal of*
875 *Geophysical Research: Solid Earth*, 102, 5005-5017,doi: 10.1029/96JB03860.

876

877

878 *Table 1: Details and references for earthquake parameters*

Earthquake	Name	Date	Latitude	Longitude	Magnitude (M _w)	Source of earthquake fault slip information
Puysegur Trench, New Zealand	PT79	12 Oct 1979	46.57°S	165.73°E	7.4	(Anderson et al., 1993)
Macquarie Ridge	MI04	23 Dec 2004	49.84°S	161.38°E	8.1	(Watson et al., 2010)
Sumatra-Anderman	SU04	26 Dec 2004	3.29°N	95.98°E	9.3	(Banerjee et al., 2007)
Northern Sumatra	SU05	28 Mar 2005	2.08°N	97.11°E	8.6	(Banerjee et al., 2007)
Southern Sumatra	SU07	12 Sep 2007	4.44°S	101.37°E	8.5, 7.9	(Konca et al., 2008)
Puysegur Trench, NZ (Dusky Sound)	PT09	15 Jul 2009	45.76°S	166.56°E	7.8	(Beavan et al., 2010)
Northern Sumatra	SU12	11 Apr 2012	2.31°N	93.06°E	8.6, 8.2	(Duputel et al., 2012, Yue et al., 2012)

879

880 *Table 2: Australian intraplate earthquakes with magnitude greater than 5.0 that have caused surface ruptures over period*
 881 *1968-2016. NB: magnitudes are as reported by Geoscience Australia following an international effort to revise historic*
 882 *earthquake magnitudes in 2016.*

Earthquake	Date	Magnitude (M _w)	Reference
Meckering, Western Australia	14 Oct 1968	6.5	(Gordon and Lewis, 1980)
Calingiri, Western Australia	11 Mar 1970	6.0	(Gordon and Lewis, 1980)
Cadoux, Western Australia	29 Jun 1979	6.1	(Denham et al., 1987)
Marryat Creek, South Australia	30 Mar 1986	5.7	(Crone et al., 1997, Machette et al., 1993, Mccue et al., 1987)
Tennant Creek (series), Northern Territory	22 Jan 1988	6.2-6.6	(Bowman et al., 1990, Crone et al., 1992, 1997)
Newcastle, New South Wales	28 Dec 1989	5.4	(Mccue et al., 1990)
Petermann Ranges, Northern Territory	21 May 2016	6.1	(Hejrani and Tkalčić, 2019, Polcari et al., 2018, Thom, 2017)

883

884

885 Table 3: Macquarie Island 2004 (MI04) earthquake coseismic offsets at GPS sites ordered by distance to MI04, uncertainties
 886 are one-sigma. Bold values are statistically significant at one-sigma.

Site	Distance from MI04 (km)	N offset (mm)	E offset (mm)	U offset (mm)
MAC1	544	4.01 ± 0.99	0.74 ± 1.48	2.80 ± 1.86
HOB2	1322	0.20 ± 1.40	5.98 ± 1.33	-1.08 ± 1.95
MOBS	1861	1.35 ± 1.51	4.20 ± 1.38	-2.18 ± 1.68
TID1	1887	1.10 ± 0.77	2.95 ± 2.01	1.58 ± 2.12
TIDB	1887	1.11 ± 0.59	3.90 ± 3.41	1.89 ± 2.65
STR1	1893	1.53 ± 0.71	3.95 ± 1.04	-0.42 ± 1.85
SYDN	1963	0.60 ± 2.69	3.17 ± 2.26	3.38 ± 3.60
CEDU	3004	1.45 ± 0.79	1.75 ± 0.93	-3.49 ± 2.42

887

888 Table 4: Parameters of best fitting viscoelastic models for horizontal and vertical components of the sites for each
 889 earthquake. [horizontal | vertical]

MI04				
Site	Elastic thickness (km)	Asthenosphere base depth (km)	Asthenosphere viscosity (10 ¹⁹ Pa s)	Upper mantle viscosity (10 ¹⁹ Pa s)
STR1	50 70	80 220	0.01 0.05	5 1
TID1	50 70	80 220	0.05 0.05	50 1
HOB2	50 90	60 220	5 0.5	4 1
SU04				
KARR	50 70	80 220	0.1 0.05	50 1
YAR2	90 70	220 220	0.5 0.05	30 1
DARW	50 50	220 80	0.5 0.01	100 500
PT09				
SYDN	50 70	80 220	0.01 0.5	10 1
TID1	90 50	100 220	5 0.05	4 1
MOBS	110 110	140 220	0.01 0.01	100 500
HOB2	90 90	220 120	1.2 0.01	1.4 10

890

891

892 Table 5: Difference in GPS site velocities calculated before and after the Macquarie Island 2004 earthquake. Uncertainties
893 are one-sigma. Pre-earthquake trend calculated over the period 2000.0 – 2004.9, and post-earthquake trend calculated
894 over the period 2004.9 – 2019.0. Sites are ordered by distance from the earthquake. Bold values are statistically significant
895 at one-sigma.

Site	Distance from MI04 eq (km)	ΔN trend (mm/yr)	ΔE trend (mm/yr)	ΔU trend (mm/yr)
MAC1	544	-2.45 ± 0.21	-1.77 ± 0.18	1.66 ± 0.49
HOB2	1322	-0.37 ± 0.23	0.23 ± 0.15	-1.87 ± 0.48
MOBS	1861	-0.21 ± 0.38	-0.34 ± 0.28	0.57 ± 0.48
TID1	1887	0.33 ± 0.23	0.07 ± 0.15	-2.40 ± 0.42
TIDB	1887	0.21 ± 0.23	0.13 ± 0.16	-2.08 ± 0.44
STR1	1893	-0.38 ± 0.36	-0.28 ± 0.26	-2.55 ± 0.48
CEDU	3004	0.18 ± 0.23	-0.20 ± 0.20	-0.96 ± 0.71
TOW2	3574	1.51 ± 0.21	0.61 ± 0.21	-1.62 ± 0.53
PERT*	4166	0.05 ± 0.36	-0.90 ± 0.34	2.27 ± 0.76
NNOR*	4198	0.30 ± 0.26	-0.40 ± 0.22	-0.02 ± 0.80
YAR2*	4397	0.70 ± 0.29	-0.16 ± 0.23	-3.15 ± 1.06
DARW*	4820	0.49 ± 0.50	-0.13 ± 0.50	2.77 ± 1.61
KARR*	4898	0.58 ± 0.28	-0.36 ± 0.19	-2.82 ± 0.65
COCO*	6791	3.17 ± 0.38	-3.29 ± 0.31	-3.99 ± 0.70
*these results may be confounded by the SU04 event				

896

897

898
899
900

Table 6: Coseismic offsets at GPS sites for the 2004 Sumatra-Anderman, 2005 northern Sumatra, 2007 southern Sumatran and 2012 northern Sumatran events, ordered by distance to SU04. Uncertainties are one-sigma. Bold values are statistically significant at one-sigma at one-sigma.

Site	Distance from SU04 eq (km)	N offset (mm)	E offset (mm)	U offset (mm)
SU04				
COCO	1709	1.96 ± 2.12	1.54 ± 1.30	0.71 ± 1.72
KARR	3492	1.35 ± 2.05	0.67 ± 0.76	1.16 ± 2.44
YAR2	4061	1.39 ± 1.02	2.25 ± 0.06	-0.24 ± 2.11
DARW	4196	3.04 ± 3.95	0.70 ± 1.76	-3.43 ± 3.14
HIL1	4325	2.42 ± 1.78	2.41 ± 2.15	-0.24 ± 2.38
PERT	4330	1.34 ± 1.07	2.00 ± 0.87	-3.66 ± 1.94
CEDU*	5402	1.02 ± 0.74	1.33 ± 0.41	-5.97 ± 2.37
TOW2	5887	3.01 ± 2.06	2.59 ± 2.10	0.54 ± 1.89
STR1*	6636	1.16 ± 0.82	3.53 ± 1.56	-1.72 ± 1.92
TID1*	6637	0.78 ± 0.70	3.19 ± 1.95	0.89 ± 2.03
HOB2	6869	1.54 ± 1.83	1.09 ± 2.00	1.05 ± 1.95
*these results may be confounded by the MI04 event				
SU05				
COCO	1575	0.98 ± 3.13	1.99 ± 1.24	2.59 ± 2.50
KARR	3316	4.27 ± 1.51	0.01 ± 0.35	-2.71 ± 1.56
YAR2	3893	3.04 ± 1.78	0.99 ± 1.07	-5.63 ± 2.63
DARW	4035	1.68 ± 1.08	-1.12 ± 1.26	0.26 ± 2.30
NNOR	4112	3.36 ± 0.99	0.87 ± 0.81	-3.56 ± 1.45
HIL1	4160	3.90 ± 1.34	2.43 ± 1.42	-1.94 ± 2.65
PERT	4164	3.54 ± 0.99	0.81 ± 0.44	-3.00 ± 0.98
CEDU	5236	2.59 ± 0.64	-1.23 ± 0.68	-2.90 ± 1.14
TOW2	5735	1.37 ± 4.32	-0.89 ± 1.43	-0.92 ± 2.65
STR1	6479	2.23 ± 0.42	-0.53 ± 0.94	0.02 ± 1.66
TID1	6481	2.57 ± 0.82	-1.92 ± 0.62	-3.17 ± 1.52
HOB2	6714	2.80 ± 1.09	-0.47 ± 2.31	-0.37 ± 1.24
SU07				
XMIS	810	2.51 ± 1.79	3.72 ± 3.45	-0.13 ± 1.7
COCO	984	2.94 ± 1.52	2.28 ± 0.79	-0.85 ± 1.84
KARR	2475	3.72 ± 0.88	1.94 ± 1.03	0.84 ± 0.81
DARW	3357	3.52 ± 0.50	0.26 ± 0.51	2.45 ± 1.83
YAR2	3059	3.45 ± 0.67	1.77 ± 1.42	0.26 ± 0.99
NNOR	3284	3.49 ± 0.74	1.37 ± 1.29	-1.04 ± 1.32
HIL1	3335	4.22 ± 0.66	2.25 ± 0.95	3.02 ± 1.55
PERT	3339	3.83 ± 0.97	1.99 ± 1.23	0.58 ± 1.70
CEDU	4443	3.18 ± 0.71	0.88 ± 0.47	0.36 ± 0.65
TOW2	5072	2.85 ± 0.54	-0.86 ± 0.65	0.44 ± 1.33
STR1	5741	2.86 ± 0.79	0.17 ± 0.70	-0.74 ± 1.47
TID1	5742	2.93 ± 0.96	1.57 ± 1.75	0.38 ± 1.31
HOB2	5967	2.56 ± 1.35	0.57 ± 1.38	1.28 ± 1.65
SU12				
COCO	1654	2.07 ± 3.95	0.76 ± 0.76	-0.70 ± 2.90

XMIS	1980	3.50 ± 3.67	-0.78 ± 3.67	0.81 ± 3.04
BRO1	3625	2.75 ± 1.54	0.97 ± 0.74	-1.04 ± 1.37
KARR	3847	3.54 ± 0.98	0.26 ± 0.83	2.28 ± 1.34
YAR2	4131	2.15 ± 1.14	2.52 ± 1.65	-0.39 ± 1.60
NNOR	4343	3.31 ± 0.61	0.62 ± 0.63	2.48 ± 2.15
HIL1	4383	3.26 ± 0.53	1.08 ± 0.95	2.07 ± 0.92
DARW	4434	-2.52 ± 3.47	-0.34 ± 1.24	0.18 ± 2.53
CEDU	5536	2.24 ± 0.69	0.56 ± 0.52	0.60 ± 1.01
TOW2	6105	2.35 ± 0.82	0.76 ± 1.05	-2.71 ± 1.35
STR1	6780	1.92 ± 0.58	0.74 ± 0.75	0.27 ± 1.24
TID1	6781	1.54 ± 0.66	0.02 ± 1.87	-1.96 ± 1.59
HOB2	6975	0.80 ± 0.74	0.42 ± 1.57	2.16 ± 1.04

901

902 *Table 7: Difference in GPS site velocities calculated before and after the Sumatra Anderman 2004 earthquake. Uncertainties*
903 *are one-sigma. Pre-earthquake trend calculated over the period 2000.0 – 2004.9, and post-earthquake trend calculated*
904 *over the period 2004.9 – 2019. Bold values are statistically significant at one-sigma.*

Site	Distance from SU04 eq (km)	ΔN trend (mm/yr)	ΔE trend (mm/yr)	ΔU trend (mm/yr)
COCO	1709	3.23 ± 0.75	-2.64 ± 0.39	-3.98 ± 0.94
KARR	3492	0.93 ± 0.42	-0.33 ± 0.34	-2.34 ± 0.84
YAR2	4061	0.59 ± 1.25	-0.33 ± 0.28	-2.53 ± 1.75
DARW	4196	0.13 ± 0.52	-0.24 ± 0.51	-2.14 ± 1.66
HIL1	4325	0.86 ± 0.52	-2.62 ± 0.67	5.37 ± 1.58
PERT^	4330	0.03 ± 0.36	-0.92 ± 0.35	-2.57 ± 0.77
CEDU*	5402	0.50 ± 0.25	-0.14 ± 0.23	-0.56 ± 0.79
TOW2	5887	1.35 ± 0.31	0.72 ± 0.29	-1.46 ± 0.68
STR1*	6636	0.31 ± 0.39	-0.28 ± 0.26	-2.55 ± 0.48
TID1*	6637	0.18 ± 0.25	0.11 ± 0.20	-1.97 ± 0.52
HOB2*	6869	-0.59 ± 0.36	0.26 ± 0.25	-0.76 ± 0.57

^this site is affected by fluid extraction (see text)

*these results may be confounded by the MIO4 event

905

906 *Table 8: Puysegur Trench 2009 earthquake coseismic offsets at GPS sites, uncertainties are one-sigma. Bold values are*
907 *statistically significant at one-sigma.*

Site	Distance from PT09 (km)	N offset (mm)	E offset (mm)	U offset (mm)
MOBS	1553	0.98 ± 0.66	0.96 ± 0.69	1.54 ± 1.33
STR1	1861	1.74 ± 0.56	0.42 ± 4.83	0.19 ± 2.85
SYDN	1868	0.33 ± 2.15	2.78 ± 5.13	0.50 ± 2.85
HOB2	1868	1.21 ± 1.79	1.73 ± 2.94	-3.13 ± 2.53
TID1	1982	2.73 ± 0.79	3.89 ± 5.00	3.26 ± 2.30

908

909 *Table 9: Difference in GPS site velocities calculated before and after the Puysegur Trench 2009 earthquake. Uncertainty is*
910 *one-sigma. Pre-earthquake trend calculated over the period 2006.0 – 2009.5, and post-earthquake trend calculated over*
911 *the period 2009.5 – 2019.0. Bold values are statistically significant at one-sigma.*

Site	Distance from Puy09 eq (km)	ΔN trend (mm/yr)	ΔE trend (mm/yr)	ΔU trend (mm/yr)
HOB2	1553	0.31 ± 0.19	-0.13 ± 0.17	-1.69 ± 0.40
TID1	1861	-0.11 ± 0.23	0.08 ± 0.26	-0.57 ± 0.69
SYDN	1868	-0.06 ± 0.22	0.38 ± 0.20	0.87 ± 0.65

MOBS

1982 **-1.16 ± 0.34** **-0.30 ± 0.24** -0.28 ± 0.60

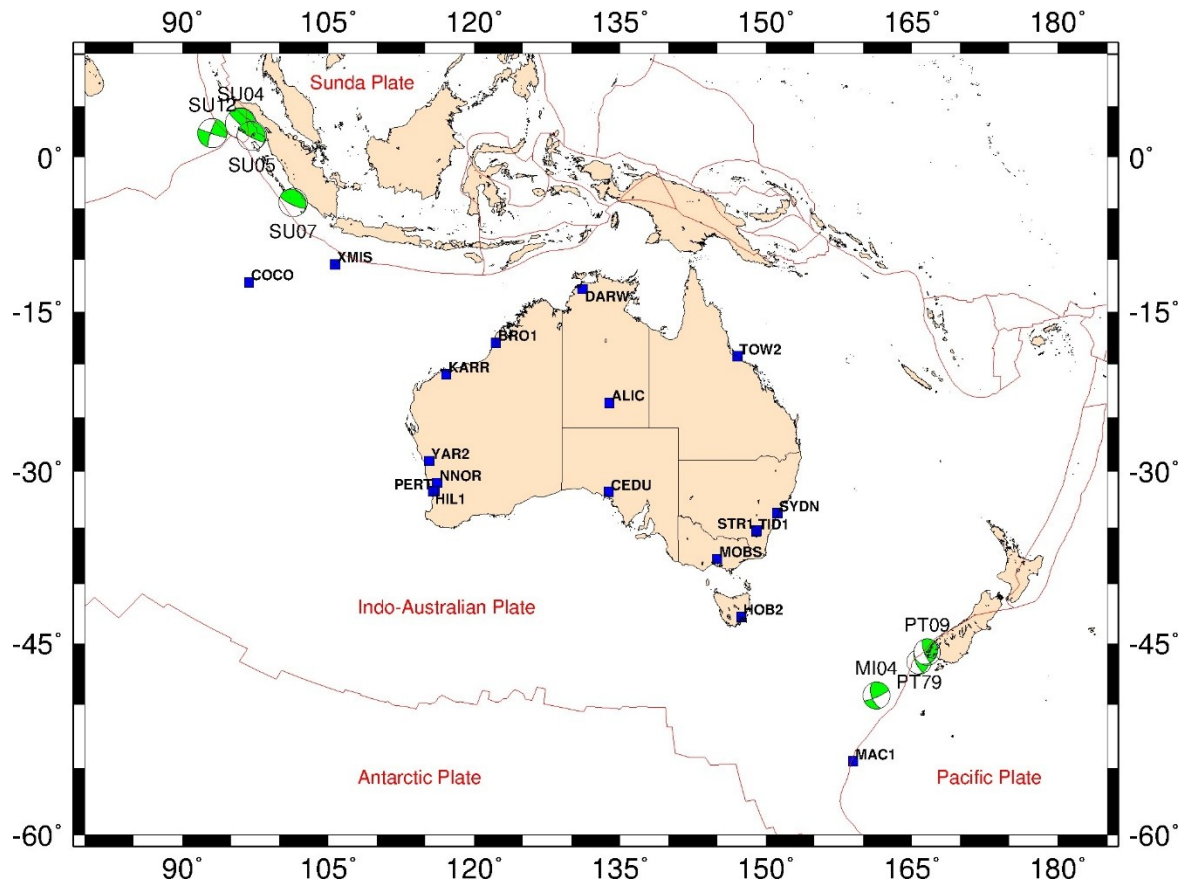
912 Table 10: Velocities of the Australian sites over the period 2000.0-2004.9, uncertainties are one-sigma. NB: MOBS and
 913 NNOR only have data from 2002.8 and 2002.5 respectively; PERT is likely undergoing increased subsidence due to local
 914 groundwater extraction (Featherstone et al., 2012). COCO and MAC1 are island sites and not included in the average values
 915 reported in the text.

Site	N (mm/yr)	E (mm/yr)	U (mm/yr)
CEDU	59.08 ± 0.21	28.98 ± 0.18	0.29 ± 0.64
COCO	50.15 ± 0.36	47.33 ± 0.30	2.20 ± 0.64
DARW	59.74 ± 0.48	36.15 ± 0.49	-3.95 ± 1.59
HOB2	55.93 ± 0.22	13.75 ± 0.14	-1.09 ± 0.52
KARR	58.28 ± 0.26	39.08 ± 0.18	1.76 ± 0.61
MAC1	33.03 ± 0.17	-10.91 ± 0.16	-3.04 ± 0.43
MOBS	57.41 ± 0.36	19.52 ± 0.27	-2.16 ± 0.46
NNOR	57.96 ± 0.24	38.51 ± 0.20	-1.12 ± 0.78
PERT	57.98 ± 0.34	39.10 ± 0.32	-5.08 ± 0.68
STR1	55.96 ± 0.35	18.51 ± 0.25	1.20 ± 0.44
TID1	55.23 ± 0.22	18.04 ± 0.13	1.07 ± 0.36
TIDB	55.35 ± 0.22	17.98 ± 0.14	0.64 ± 0.38
TOW2	55.35 ± 0.20	28.68 ± 0.20	0.66 ± 0.50
YAR2	57.36 ± 0.29	38.95 ± 0.21	1.55 ± 0.70

916

917

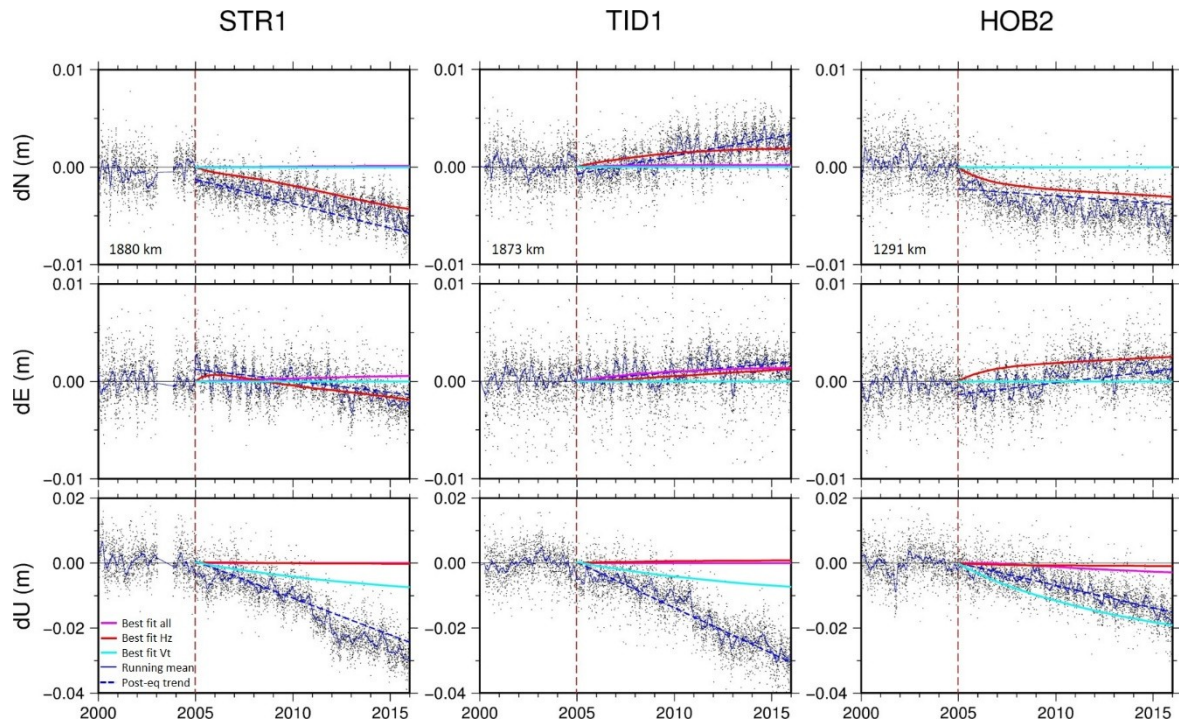
918



919

920 *Figure 1: Indo-Australian tectonic plate setting including the focal mechanisms of the earthquakes investigated in this study*
 921 *(the two digits in the EQ label reflect the year of occurrence), Australian GPS sites are shown as blue squares. Plate*
 922 *boundaries are in red (Bird, 2003).*

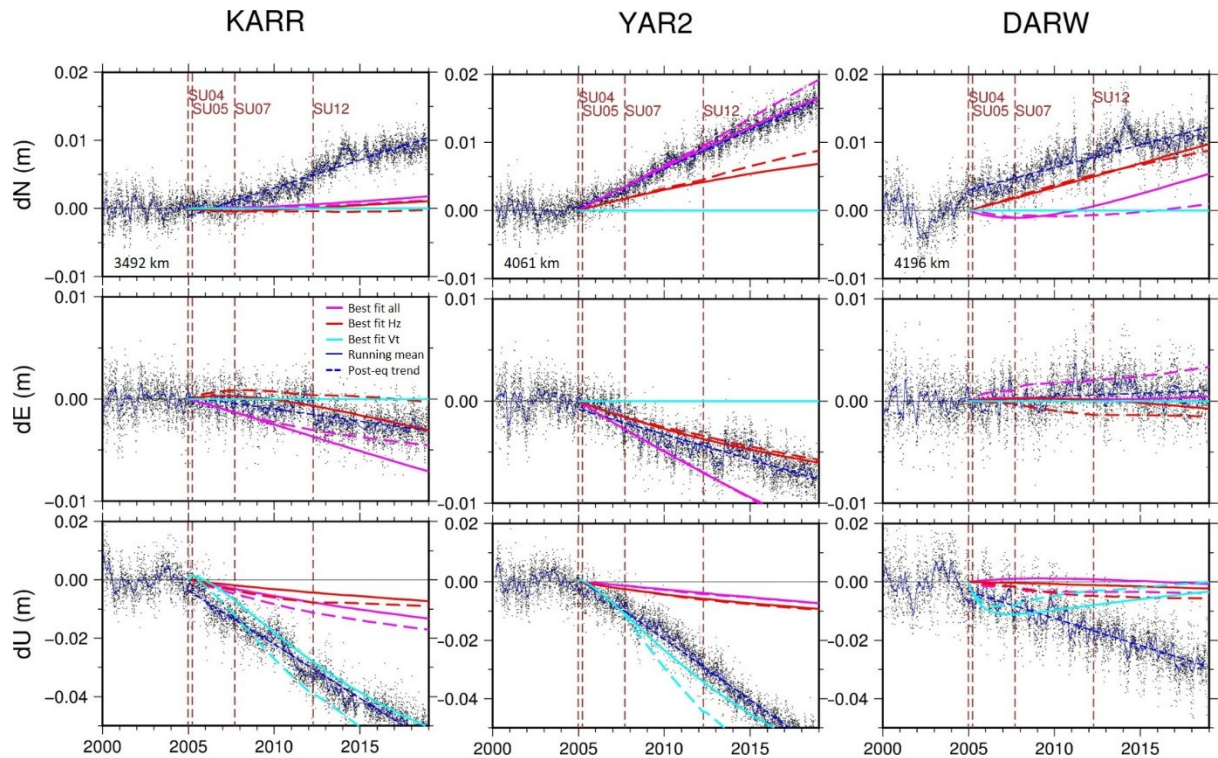
923



924

925 *Figure 2: GPS time series at Mt Stromlo (STR1), Tidbinbilla (TID1), and Hobart (HOB2) after removing the trend computed*
 926 *over the pre-earthquake period (2000.0–2004.9). A 100-day running mean is shown in solid blue. Blue dashed line is the*
 927 *estimated linear velocity post-earthquake. Red is the best fitting viscoelastic model for the horizontal components, cyan is*
 928 *the best fitting viscoelastic model for the vertical component and magenta is the best fitting viscoelastic model for all*
 929 *components. The dashed vertical line indicates the date of the Macquarie Island earthquake (23 December 2004). The value*
 930 *in the bottom left of the upper panels is the distance of each site from the earthquake surface epicentre. Coseismic offsets*
 931 *have been removed.*

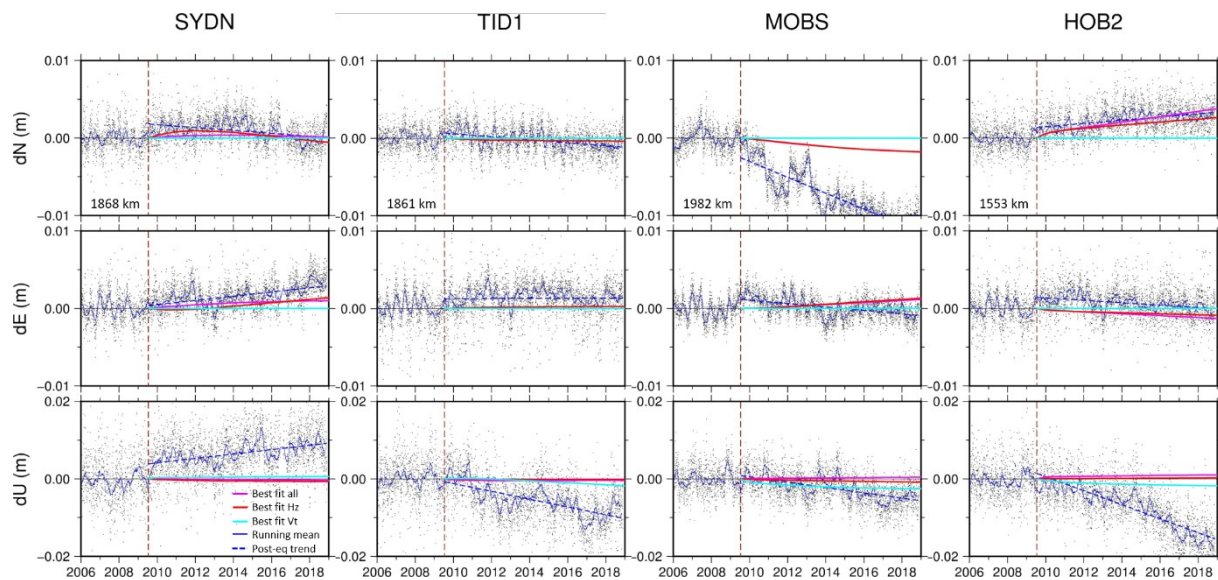
932



933

934 Figure 3: GPS time series at Karratha (KARR), Yarragadee (YAR2), and Darwin (DARW) after removing the trend computed
 935 over the pre-earthquake period for SU04 (2000.0–2004.9). A 100-day running mean is shown in blue. Blue dashed line is the
 936 estimated linear velocity post-earthquake. The solid lines of the viscoelastic models are for SU04 only, the dashed lines
 937 incorporate the combined response of all four Sumatran earthquakes. The brown dashed vertical line indicates the date of
 938 the earthquakes. Coseismic offsets have been removed.

939



940

941 Figure 4: GPS time series at Sydney (SYDN), Tidbinbilla (TID1), Melbourne (MOBS), and Hobart (HOB2), detrended over the
 942 pre-earthquake period (2006.0–2009.5). 100 day running mean is plotted in blue. Blue dashed line is the estimated linear
 943 velocity post-earthquake. Red is the best fitting viscoelastic model for the horizontal components, cyan is the best fitting
 944 viscoelastic model for the vertical component and magenta is the best fitting viscoelastic model for all components. Dashed
 945 vertical line indicates the date of the Puysegur earthquake (15 July 2009). The value in the bottom left of the upper panels is
 946 the distance of each site from the earthquake surface epicentre. Coseismic offsets have been removed.

947